1

Casting, Moulding and Forming

Process capability study of hybrid investment casting

Rupinder Singh[1]
[1] Dept. of Production Engineering, Guru Nanak Dev Engineering College, Ludhiana-141006, India

Abstract. The purpose of the present study is to investigate process capability of hybrid investment casting (HIC) for industrial applications. Starting from the identification of component, prototypes were prepared as replicas of plastic patterns (by hybridization of fused deposition modelling and conventional investment casting). Some important mechanical properties were also compared to verify the suitability of the components. Final components produced are acceptable as per ISO standard UNI EN 20286-I (1995). The results of study suggest that HIC process lies in ±4.5sigma (σ) limit as regard to dimensional accuracy of component is concerned. This process ensures rapid production of pre-series technological prototypes and proof of concept at less production cost and time.

Keywords: Hybrid investment casting, process capability, dimensional tolerance.

1. Introduction

The process of casting metal into a mould produced by an expendable pattern with a refractory slurry coating (sets at room temperature), after which the wax pattern is removed through the use of heat prior to filling the mould with liquid metal is known as investment casting (IC)/lost wax process [1,2]. It is one of the economical, mass-production casting processes [2,3].

With the industry growing at a very fast pace reduced production time is a major factor in industries to remain competitive in the market place [4]. Therefore traditional product development methodology has given way to rapid fabrication techniques like rapid prototyping [5]. HIC (Hybridization of fused deposition modelling (FDM) and IC) is one of the rapid manufacturing technique which enables near net shaped metal parts containing complex geometries and features from a variety of metals. FDM forms three-dimensional objects from CAD generated solid or surface models. In this process, FDM material like ABS, elastomer, polycarbonate etc. feeds into the temperature-controlled FDM extrusion head, where it is heated to a semi-liquid state [5]. The head extrudes and deposits the material in thin layers onto a fixtureless base. The head directs the material into place with precision, as each layer is extruded, it bonds to the previous layer and solidifies [6]. The designed object emerges as a solid three-dimensional part/pattern without the need for tooling [7]. Fig. 1 shows schematic of FDM.

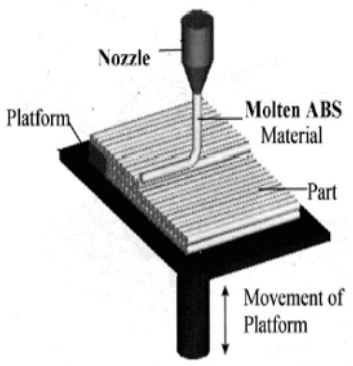

Fig.1. FDM schematic [7]

Individual patterns are attached onto a common wax sprue system to form a cluster in the form of tree. The cluster is repeatedly dip coated in investment slurry containing graded suspensions of refractory particles and followed by stucco application to build shell thickness and strength [8]. When dried, the ABS pattern is melted out via autoclaving to reveal the internal cavities of the ceramic shell. The first layer is normally a fine coating so that a good surface finish on the casting will be obtained. Subsequent layers are made up of ceramic slurry and refractory granules. The shell will normally be made up of between five and eight layers depending on the cooling rate required and the subsequent metallurgical properties [9-10].

The literature review reveals that lot of work has been reported on IC, its applications by different researchers [10,12]. But very few authors have reported on hybridization of IC and FDM process in ordere to get good quality casting. The main objective of this research paper is to study the process capability of HIC. In order to accomplish this objective, 'plain carbon steel casting' has been chosen as a benchmark (Ref. Fig. 2). The chemical

S. Hinduja and L. Li (eds.), *Proceedings of the 37th International MATADOR Conference*,
DOI: 10.1007/978-1-4471-4480-9_1, © Springer-Verlag London 2013

composition of plain carbon steel was C=0.43%, S=0.017, P=0.023, Si= 0.35 and Mn=0.75. The component selected is a outer cover of memory stick.

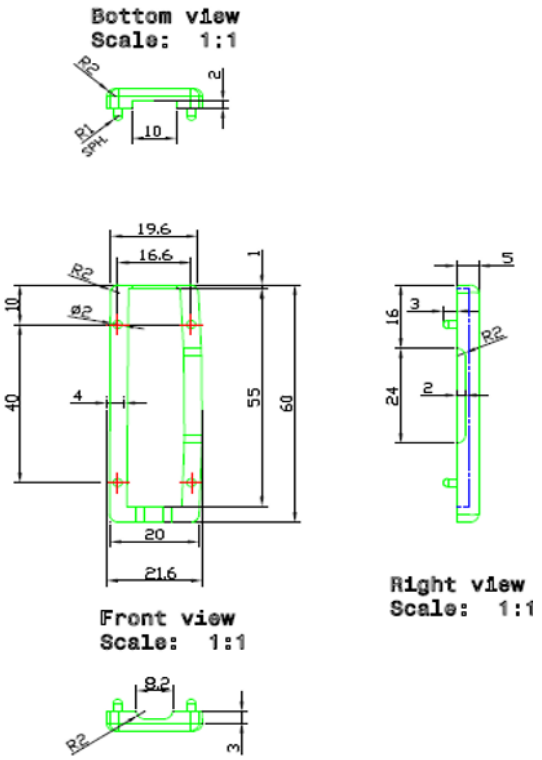

Fig.2. Benchmark dimensions

CAD model (Fig. 2) of the bench mark was made on UNIGRAPHICS software. The 3D CAD model was converted into the STL format which was fed into the computer attached to the FDM machine. The machine was cleaned and the benchmark was set in various orientations. After setting of orientations the component was sliced, layer by layer construction was done and thereafter the components were cleaned. Fig. 3 shows ABS pattern prepared by FDM.

Fig.3. ABS pattern prepared by FDM

2. Experimentation

As a usual practice in industry, for IC three different types of layers; primary (1°), secondary (2°) and tertiary (3°) are applied on shells (as fine, semi coarse and coarse grains of slurry). It should be noted that the number of layers (5-8) are dependent on size/volume/ weight of casting and can't be generalised. Based upon pilot experimentation it has been observed that for present case study five layers are providing sufficiently good results (acceptable as per industrial requirements) in terms of surface finish (Ra5.51-6.02µm) and hardness (195-205HV) etc. On the basis of the results obtained as above it was decided to prepare the shell with minimum five layers.

Finally castings produced from plain carbon steel were measured for dimensional accuracy with the help of CMM (Ref. Fig. 2). The observations are shown in Table 1 for four critical dimensions (D1 = 60mm, D2 = 3mm, D3 = 10mm and D4= 21.6 mm). The dimensional data has been collected and analyzed; for the critical dimensions D1, D2, D3 and D4 (Ref. Table 1) by preparing 16 samples of HIC. Table 2 shows the classification of different IT grades according to ISO UNI EN 20286-I (1995) for D1, D2, D3 and D4.

Now for a generic nominal dimension D_{JN}, the number of the tolerance units is evaluated as [13,14]:

$$n= 1000(D_{JN} - D_{JM})/ i,$$

Where D_{JM} is a measured dimension

$$\text{Tolerance factor } i = 0.45 (D)^{1/3} + 0.001D,$$

Where, D is the geometric mean of the limiting values.
In present case for nominal dimension (12.46mm):

$$D = (10x\ 18)^{1/2} = 13.416 \text{ mm}$$
$$i = 0.45 (D)^{1/3} + 0.001D$$
$$= 0.45 (13.416)^{1/3} + 0.001(13.416)$$
$$= 1.082964$$

For casting obtained from 12mm shell thickness:

$$n = 1000(D_{JN} - D_{JM})/ i$$
$$= 1000(12.46-12.301)/1.082964$$
$$=147$$

The component selected in present study is actually prototype of memory stick cover and dimensions (D1, D2, D3 and D4) was chosen for demonstration over the rest of the dimensions for the measurement and comparison purpose because it is actually mating/functional dimension in assembly. It should be noted that the results are based upon study performed on a simple geometry (Ref. Fig.2), but the same results are applicable to any complex geometry of similar volume as

because solidification time depends upon ratio of volume to surface area.

Table 1. Measured dimensions for process capability analysis

Sample No.	D1=10 mm	D2=3 mm	D3=60 mm	D4=21.6 mm
1	9.9216	3.0203	59.8100	21.7129
2	9.9506	2.9710	59.8575	21.7534
3	10.0791	3.0508	59.8901	21.6734
4	10.0335	3.0510	59.8248	21.5921
5	9.9713	2.9559	59.9080	21.6939
6	9.9689	3.0754	60.0500	21.6578
7	10.0276	3.0102	59.9222	21.6718
8	10.0738	3.0247	59.8851	21.5934
9	10.0324	3.0300	60.0223	21.6820
10	9.9470	3.0503	59.8313	21.5977
11	10.0279	2.9776	59.9782	21.6119
12	10.0113	3.0152	59.8908	21.6988
13	10.0228	3.0318	59.9178	21.6366
14	9.9813	2.9812	59.8534	21.6191
15	10.0332	3.0777	59.9575	21.6225
16	9.9786	3.0258	59.8974	21.6811

Table 2. IT grades for measured dimensions

Sample No.	IT Grade for D1	IT Grade for D2	IT Grade for D3	IT Grade for D4
1	IT11	IT10	IT10	IT10
2	IT10	IT11	IT10	IT11
3	IT11	IT12	IT9	IT8
4	IT9	IT12	IT10	IT9
5	IT9	IT12	IT9	IT9
6	IT9	IT13	IT7	IT7
7	IT9	IT9	IT8	IT8
8	IT11	IT10	IT9	IT9
9	IT9	IT11	IT5	IT8
10	IT10	IT12	IT10	IT9
11	IT9	IT10	IT5	IT8
12	IT7	IT9	IT9	IT9
13	IT9	IT60	IT9	IT7
14	IT8	IT10	IT10	IT7
15	IT9	IT13	IT7	IT7
16	IT8	IT10	IT9	IT8

3. Results and Discussion

Based upon observations in Table 1, capability analysis calculations have been made to assess whether a system is statistically able to meet a set of specifications or requirements. The comparison is made by forming the ratio of the spread between the process specifications (the specification "width") to the spread of the process values, as measured by 6 process standard deviation units (the process "width"). The capable process is one where almost all the measurements fall inside the specification limits. The Capability Indices (Cp) index is used to summarize a system's ability to meet two-sided specification limits (upper and lower). However it ignores the process average and focuses on the spread. If the system is not centered within the specifications, Cp alone may be misleading.

$$Cp = \frac{\mathrm{USL} - \mathrm{LSL}}{6\sigma} \qquad Cpk = min\left[\frac{USL-\mu}{3\sigma}, \frac{\mu - LSL}{3\sigma}\right]$$

Where: USL = upper specification limit, LSL= lower specification limit, σ = standard deviation, μ = mean of data.

The higher the Cp value the smaller the spread of the system's output. Cp is a measure of spread only. A process with a narrow spread (a high Cp) may not meet customer needs if it is not centered within the specifications. Cp should be used in conjunction with Cpk to account for both spread and centering. Cp and Cpk will be equal when the process is centered on its target value. If they are not equal, the smaller the difference between these indices, the more centered the process is. Cpk is a capability index that tells how well as system can meet specification limits. Since it takes the location of the process average into account, the process does not need to be centered on the target value for this index to be useful. If Cpk is 1.0 the system is producing 99.73% of its output within specifications. The larger the Cpk, the less variation you will find between the process output and specifications. If Cpk is between 0 and 1.0 not all process output specifications meets. For process capability analysis Table 3 shows summary of statistical analysis for nominal dimension D1, D2, D3 and D4.

Table 3. Statistical analysis for nominal dimensions

Statistical analysis	D1	D2	D3	D4
Cp	1.5658	1.3825	1.5833	1.6631
Cpk	1.5375	1.2239	1.1918	1.5557
Mean of data	10.0038	3.021	59.906	21.65
Lower spec. limit (LSL)	9.79	2.81	59.62	21.39
Upper spec. limit (USL)	10.21	3.19	60.38	21.89
Min. value	9.9216	2.9559	59.81	21.5921
Max.value	10.0791	3.0777	60.05	21.7534
Standard deviation	0.04540	0.0359	0.068	0.0477
Range	0.1575	0.1218	0.24	0.1613

Figs. 4-6 shows R chart, X chart and process capability histogram for nominal dimension D1. As observed from

Figs. 4-6, for Cpk value of 1.5, the area under normal curve is 0.999993198 and non conforming ppm is 6.8016. Similarly Cp and Cpk values for other dimensions (D2, D3 and D4) were calculated. The value of Cpk for all critical dimensions is 1.33. The results of study suggest that RSM process lies in ±4.5sigma (σ) limit as regard to dimensional accuracy of plastic component is concerned.

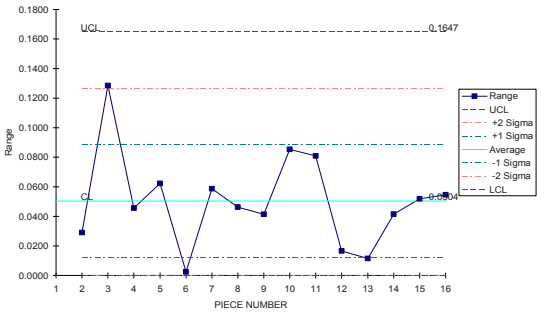

Fig. 4. R chart for nominal dimension D1

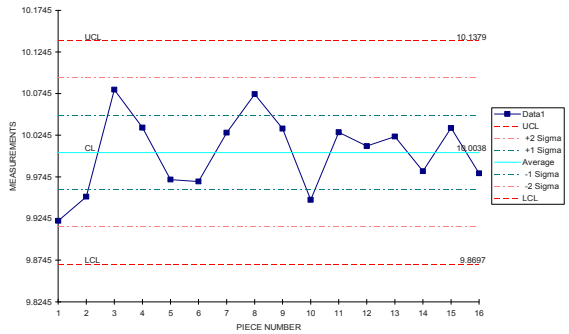

Fig. 5. X chart for nominal dimension D1

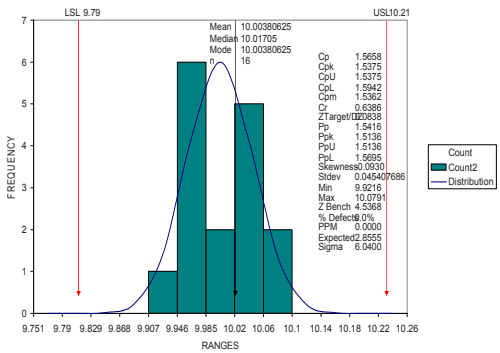

Fig. 6. Process capability histogram for nominal dimension D1

4. Conclusions

On the basis of experimental observations it can be concluded that HIC is highly capable process. It is observed that the 'Cpk value' for all the four critical dimensions in the present study is 1.33. As Cpk values of 1.33 or greater are considered to be industry benchmarks, so this process will produce conforming products as long as it remains in statistical control. The IT grades of the components produced are consistent with the permissible range of tolerance grades as per ISO standard UNI EN 20286-I (1995). The adopted procedure is better for proof of concept and for the new product, for which the cost of production for dies and other tooling is more.

Acknowledgments: The author is thankful to DST, New Delhi for financial support.

References

[1] Wang S., Miranda A. G., and Shih C., (2010) A Study of Investment Casting with Plastic Patterns. Materials and Manufacturing Processes 25(12): 1482-88.

[2] Chattopadhyay H., (2011) Estimation of solidification time in investment casting process. The International Journal of Advanced Manufacturing Technology 55(1-4): 35-38.

[3] Rafique M.M.A. and Iqbal J., (2009) Modeling and simulation of heat transfer phenomena during investment casting. International Journal of Heat and Mass Transfer 52(7-8): 2132-2139.

[4] Singh R., (2010) Three dimensional printing for casting applications: A state of art review and future perspectives. Advanced Materials Research 83-86: 342-349.

[5] Chhabra M. and Singh R., (2011) Rapid casting solutions: a review. Rapid Prototyping Journal 17(5): 328-350.

[6] Garg H. and Singh R., (2011) A Framework for Development of Pattern for Dies Using Fused Deposition Modeling. International Journal of Advanced Mechatronics and Robotics 53-60.

[7] Garg H. and Singh R., (2012) Experimental investigations for development of pattern for dies using FDM. Materials Science Forum, Special topic volume: Rapid casting solutions 701: 77-83.

[8] Mishra S. and Ranjana R., (2010) Reverse Solidification Path Methodology for Dewaxing Ceramic Shells in Investment Casting Process. Materials and Manufacturing Processes 25(12): 1385-88.

[9] Sidhu B. S., Kumar P. and Mishra B.K., (2008) Effect of slurry composition on plate weight in ceramic shell investment casting. Journal of Materials Engineering and Performance 17: 489–498.

[10] Kumar S., Kumar P. and Shan H.S., (2006) Parametric Optimization of Surface Roughness Castings Produced by Evaporative Pattern Casting process. Mater. Lett. 60: 3048–3053.

[11] Norouzi Y., Rahmati S., Hojjat Y., (2009) A novel lattice structure for SL investment casting patterns. Rapid Prototyping Journal 15(4): 255 – 263

[12] Konrad C.H., Brunner M., Kyrgyzbaev K., Völkl R., Glatzel U., (2011) Determination of heat transfer coefficient and ceramic mold material parameters for alloy IN738LC investment casting. Journal of Materials Processing Technology 211(2): 181-18

[13] UNI EN 20286-1 (1995) ISO system of limits and fits, Bases of tolerances, deviations and fits.

[14] Devor R. E., Chang T., and Sutherland J. W., (2005)Statistical quality design and control contemporary concepts and methods, Pearson Prentice Hall (Second edition) New Jersey.

Enhancing the performance of laboratory centrifuges with carbon fiber rotors

U. Klaeger[1] and V. Galazky[2]
[1] Fraunhofer Institute for Factory Operation and Automation IFF, Magdeburg, Germany
[2] carbonic GmbH, Magdeburg, Germany

Abstract. Centrifuges have multiple uses in medicine and in laboratories, most notably to separate substances such as blood plasma and serums. A centrifuge's rotors hold sample containers. Centrifugal forces equaling 25,000 times the force of gravity act on rotors and samples at speeds of 20,000 rpm. Unlike present conventional solutions (rotors made of special aluminum alloys), the load-bearing structures of the lightweight rotors presented here are made of carbon fiber-reinforced polymers (CFRP). The complex rotor and mold geometries are selective laser sintered. Given the fibers' extremely high load-bearing capacity, lightweight rotors manufactured with this novel technology set new standards for weight, stability and service life compared to current concepts. Moreover, this can reduce the warm-up time typical for aluminum rotors by at least fifty percent.

Keywords: Composite and Polymer Manufacturing, Additive Manufacturing, Forming Processes, Carbon Fiber Material, Centrifuges, Design.

1. Introduction

Centrifugation is the process most frequently applied to separate materials in liquids. Most notably, they are used to separate materials, e.g. blood plasma and serums, and produce genetically engineered substances.

A centrifuge consists of housing, a drive unit with controller, a rotor, a safety enclosure and, frequently, a cooling system. The rotor holds sample containers. There are rotors for different sizes of samples (from the microliter range to one liter) and numbers of sample containers (depending on the task). They are subjected to extreme mechanical loads. Technically this makes them core centrifuge components.

During centrifuging, a solution's solid constituents precipitate under the effect of a stronger gravitational field produced by the centrifugal forces generated by rapid rotation. In this stronger gravitational field, constituents with greater mass displace lighter particles, which are thrust closer to the axis of rotation. The gravitational force increases exponential to the distance from the axis of rotation (radius). Superior centrifuges operate at high speeds of frequently more than 20,000 rpm. This produces gravitational fields, which exceed normal gravitation several thousands of times over. Conventional rotors are made of special aluminum alloys. They are relatively easy and cheap to manufacture but have drawbacks in terms of their stability and attainable rotational speeds. In addition, undesirable imbalances frequently appear.

Therefore, lightweight rotors are alternatively made of fiber composite materials. A variety of methods exist but, at present, only rotors with resin transfer molded bodies and wound highly stressed annular shells are commercially available.

Admittedly, lightweight rotors made entirely or partially of carbon fiber-reinforced polymers or mixed are more expensive than conventional aluminum rotors since they are predominantly manufactured by hand. However, in addition to having a substantially lower density, they weigh far less and are approximately six times more stable than aluminum rotors.

Lower weight cuts centrifuges' energy consumption and ramp-up times and also reduces an overall centrifuge system's mechanical loads. In addition, lighter CFRP rotors simplify handling since aluminum rotors often weigh up to 50 lbs.

2. Motivation and aims

The authors jointly developed a method of manufacturing lightweight rotors from pre-molded woven carbon fibers. Carbon fibers have high tensile strength, provided the fibers are aligned with the direction of load. They are thusly processed relatively easily when profiles are long and shapes are flat or cylindrical.

However, tapering and freeform surfaces like those of centrifuge rotors are more complicated since the fibers are unable to adhere to these surfaces and slip easily. Hence, rotors are only wound at present.

The drawback of this is that the fibers cannot be aligned with the direction of load. Further, the manufacture of wound rotors requires extremely expensive multi-axis winders and wound surfaces are never really smooth. This affects a rotor's running smoothness adversely.

The new methods of positioning fibers aligned with the direction of load on conical surfaces employs carbon spiral tapes that exact match the winding of a rotor's tapered surface geometrically. In a first step, a base body that holds sample containers and a hub with a conical exterior shape are manufactured. Then, the spiral tape is placed around the base body.

Since the geometry of the spiral tape and base body corresponds, the spiral tape stays in place and only the two ends of the tape have to be secured with some spray adhesive. The base body layered with spiral tape is placed in a second mold and impregnated with resin by RTM. This design reduces the moment of inertia by more than half.

The complicated design principal considered by these authors requires suitable forming tools that reproduce the complex geometries (e.g. undercuts). Therefore, generative (laminate) methods of geometry generation are used to make molds. Given their practically unlimited freedom of design, these technologies can, for instance, already produce close-contour cooling channels during mold making. Furthermore, selective laser sintered, geometrically complex inserts reduce the weight of rotor bodies.

When this novel concept is successfully implemented, a lighter weight CFRP rotor will be at least 10% more stable than a lightweight wound rotor. At the same time, it can be expected to have a permissible speed that is at least 10% higher than that of lightweight rotors in the same class. First, comprehensive physical models and new calculation algorithms for the FEM analysis were developed, which ensure that lightweight rotors can be manufactured reproducibly for future implementation in practice.

3. Conceptual design of the manufacturing technology

First, the CAD models of the two sizes of CFRP rotor analyzed (14 x 50 ml and 6 x 500 ml) were generated. They served as the basis for subsequently calculating the shell design and potential failure criteria (maximum stress, maximum strain, etc.) based on the finite element method (FEM), Fig. 1.

The ANSYS analysis package was used for the calculations since it contains tools that are especially effective for the calculating the structures of fiber composite materials.

This tool was also used to identify and calculate the principal stresses produced during centrifugation and the resultant critical zones in the rotor geometry (Fig. 2).

Taking the properties required of the rotor as the point of departure, the energy of three different rotor geometries was analyzed in order to draw conclusions about the rotational energy of each. The goal targeted for the overall system was 94,000 Nm. Only the variant "Core 2" met this goal (see Table 1).

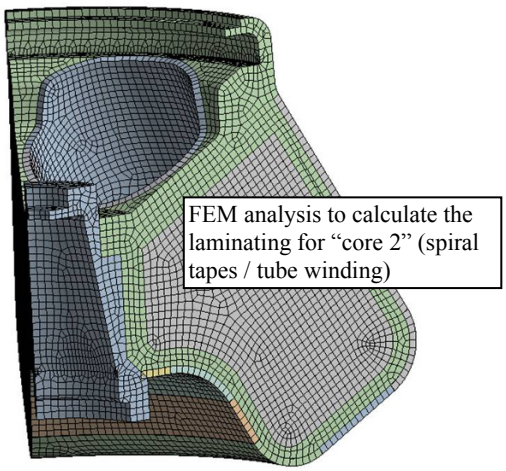

Fig.1. Rotor design calculation and simulation

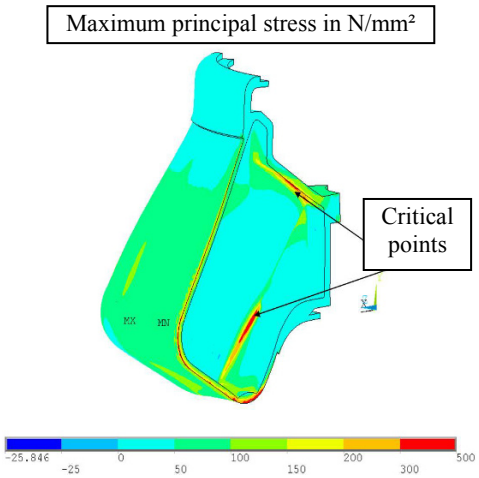

Fig 2. Critical rotor geometry zones.

Since the geometry had not been optimized, designing the rotor geometry as a monolithic CFRP block even worsened the initial values.

The simulation determined that CFRP rotors weigh up to 44% less because they have a lower density (approximately 1.5 g/cm³ at a content of approximately 60% fiber by volume) than aluminum (ca. 2.7 g/cm³) rotors.

This weight advantage shortens acceleration and deceleration time while retaining a centrifuge's performance. Consequently, cycle times are shorter.

Table 1. Energy analysis of a 6 x 500 ml CFRP rotor compared with an aluminum rotor

Rotational energy [Nm]			
Type	**Rotor**	**Target**	**Difference**
Aluminum	154,246	94,000	60,246
Monolithic CFRP	158,913	94,000	64,913
Core 1-foam	135,208	94,000	41,208
Core 2-SLS	86,426	94,000	-7,574

In addition, higher speeds can be run, thus increasing the relative centrifugal acceleration. Moreover, this weight reduction makes such rotors easier to handle. Their resistance to corrosion and enhanced fatigue strength are additional advantages.

4. Forming tool design

Taking the calculation results as the starting point, so-called displacers (as inserts) for the rotor casting mold were designed and laser sintered (Fig. 3a).

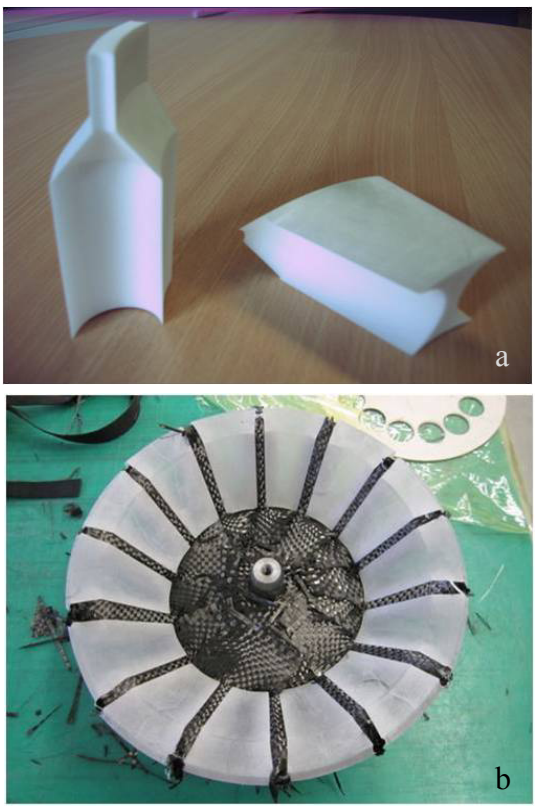

Fig 3. Selective laser sintered master models displacersas the basis for silicone molds (a). Rotor variant Core 2 with 14 inserted SLS cores (b).

In addition to cutting weight, such laser sintered inserts significantly reduced the rotational energy. Arranged in position, the inserts are intended to assure Core 2 has the rotational energy desired.

The prototyping technologies of selective laser sintering and vacuum casting were combined in order to deliver the large quantities required. The overall design was simultaneously optimized for fiber composites. The prototyping technologies of selective laser sintering and vacuum casting were combined in order to deliver the large quantities required. The overall design was simultaneously optimized for fiber composites.

5. Laboratory prototype and mold making

The results of these tests entered into the development of the manufacturing technology to properly design the future forming tool for casting.

Taking the theoretical calculations as the starting point, initial rotor prototypes were subsequently produced to verify the variance analysis. This entailed producing laminating molds to assure the reproducibility of the manufacturing in certain quantities. One of the first rotor prototypes is pictured in Fig. 3b.

The complete lightweight rotor consists of nine different components, including the aerosol ring, hub, rotor and six filling elements. The filling elements are hidden in the rotor housing between the sample container holders and are made of a lightweight plastic, thus reducing the lightweight rotor's weight.

The hub is force fit with the lightweight rotors while it is being manufactured/layered. The use of two different hubs is planned at present. The aerosol ring is separately made of plastic and subsequently bonded to the rotor once it has been manufactured. The greatest challenge during development was reconciling the design of forming tools with the layering technology to be developed (Fig. 4).

Fig 4. Elements of the casting mold for the first rotor prototypes.

The forming tool must have the rotor's geometric complexity and its design must facilitate the defined fiber layering, which is crucial to facilitating full impregnation and a uniformly high content of fibers by volume.

These are essential for the manufacture of extremely stable rotors. Therefore, the development partners employed simulation methods to optimize the layering technology and to design the forming tools.

The tests executed made it possible to implement design modifications in a matter of hours, thus enabling the development partners to rapidly find and test solutions to the most complicated layering steps. The first proposed solution for the carbon fiber rotor is depicted in Fig. 5.

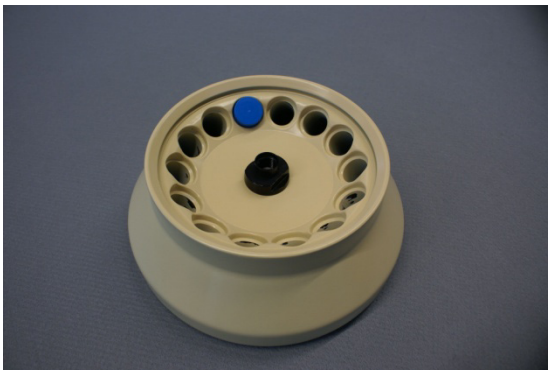

Fig 5. First solution for the carbon fiber rotor.

6. Conclusion

The extensive work to design and develop the layering technology delivered findings that enabled carbonic GmbH to completely engineer its manufacturing processes without having to modify the mold's design.

Rotors manufactured with the new methods combine the smooth surface of aluminum rotors with the advantages of wound rotors, e.g. lower weight and better fracture characteristics. The new lightweight rotors weigh up to fifty percent less than aluminum rotors and can withstand up to twenty percent higher loads.

Compared with wound rotors, the new methods can produce smaller quantities more cost effectively. Further, rotors manufactured with the new methods are more stable and have a smoother surface, which enables rotors to operate smoothly.

Acknowledgements: Support for this project came from the Investitionsbank of Saxony-Anhalt, for which the authors express their sincere thanks.

References

[1] Beckwith, S., Hyland, C., SAMPE Journal, Vol 34, No. 6, (1998) Resin Transfer Moulding: A decade of technology advances. 7-19

[2] VDI-Richtlinie 3404, Beuth Verlag Berlin (2009) Additive fabrication: Rapid technologies (Rapid Prototyping)

[3] DIN EN 3783, Beuth Verlag Berlin (1992) Aerospace series: fibre composite materials; normalization of fibre dominated mechanical properties

[4] DIN 58970-1, Beuth Verlag Berlin (1996) Laboratory centrifuges-Part 1: Definitions, testing, marking

[5] DIN 58970-2, Beuth Verlag Berlin (1998) Laboratory centrifuges; centrifuge tubes for relative centrifugal acceleration up to 4000.

Composite grid cylinder vs. composite tube: Comparison based on compression test, torsion test and bending test

Lai C.L., Liu C. and Wang J. B.
Shaanxi Engneering Research Center for Digital Manufacturing Technology, Northwestern Polytechnical University, Xi'an 710072, China

Abstract: The use of composite grid cylinder, which is known for its very high strength/stiffness-to-weight ratio, gives large weight savings over metallic. However, the mechanical property comparison between composite grid cylinder and traditional composite tube is lake of research. To better quantify the advantages or disadvantages between the composite grid cylinder and the composite tube, this paper describes the fabrication and the test of composite grid cylinder and composite tube. Composite grid cylinders are fabricated manually guided filament winding. And composite tube is fabricated by autoclave moulding. In order to evaluate structure mechanical property, comparison including compression test, torsion test and bending test, are carried out. Finally, comparison results show that strength to weight ratio of composite grid cylinder is lower than composite tube, but stiffness to weight ratio is 2.7 times higher than composite tube in bending test.

Keywords: Composite grid cylinder, Composite fabrication, Mechanical property comparison

1. Introduction

The Composite grid cylinder is characterized by a lattice of rigid, interconnected rids.It consists of a dense system of unidirectional composite helical, circumferential or axial ribs and mainly derive its strength and stiffness form ribs. Because composite grid cylinders are attractive structures for application in aerospace from their high strength/stiffness to weight ratio, high impact resistance and low fabrication cost, they have been successfully applied to interstages, payload adapters[1-4] and fairings of launch vehicles [5,6], and expanded to fuselage section [4]. But all the applications only exploit high load carrying capacity of the structure in axial direction. The potential of beam application which carry torsional load and bending load is lack of research.

Composite tubes, which have more second axial moment of area and can provide higher bending stiffness and torsion stiffness than other solid structure, have been used in spacecraft truss and solar unmanned air vehicle beams [7, 8]. However, in contrast to the composite laminate tube with finite thickness whose mass cannot be reduced beyond some minimum value determined by the finite thickness of the ply, the mass of gride cylinders is governed by the rib spacing and cross-sectional area and can be readily reduced to a desirable value.

In this research, composite grid cylinders and composite tubes for comparison testing are fabricated using the same materials. Comparison testing schemes, including axial compression testing, torsion testing and bending testing, are modified in consideration of test specimen features and test situations. Finally, their compression property, torsion property and bending property are compared and analyzed.

2. Specimen manufacturing

Composite tubes are made by prepreg sheet, cured in autoclave. Layup is $[45/-45/45/-45/0_4]s$, and the thickness of each ply is about 0.125 mm. Carbon fiber is CCF300-3K carbon fiber, and resin matrix is high temperature epoxy resin. The measured data of the main parameters are shown in Table 1.

Table 1. Composite tube specimen parameter

Specimen	Length (mm)	Outer diameter (mm)	Inner diameter (mm)
Compression	98	40.5	36.3
Bending	373	40.8	36.6
Torsion	355	40.6	36.4

Composite grid cylinders are made by continuous wet winding during which impregnated carbon tows are placed into helical and circumferential grooves formed on the surface of the mandrel with the aid of:

- Machining of the foam core covering the mandrel.
- Forming grooves in the silicon rubber elastic coating that is pulled out of the structure after curing.
- Forming grooves in thin metal or wooden panels mounted on the mandrel surface [2].

The second method, using the silicon rubber elastic coating, provides two additional advantages. The silicon rubber elastic coating is typically a high thermal expansion. It provides lateral compaction to the ribs during curing. In addition, after the structure is cured, it is easy to remove the mandrel and the rubber coating can be pulled out facilely. In this research, composite grid cylinders are made by continuous wet winding, using the silicon rubber elastic coating, and cured in high temperature stove. The materials for composite grid cylinders are the same as composite tube. CCF300-3K carbon fiber is adopted, and high temperature epoxy resin is used for the resin matrix. The typical manufacturing process involves the following operations

- Forming of the silicon rubber elastic coating
- Wet winding of ribs.
- Curing.
- Machining of the rings.
- Removal of the mandrel and the elastic coating.

In general, composite grid cylinders are haracterized with eight design variables (shown in Fig. 1), i.e.,

- D-structure outer diameter.
- L-structure length.
- a_h-spacings of the helical ribs.
- a_c-spacings of the circumferential ribs.
- b_h-widths of helical rib.
- b_c-widths of circumferential rib.
- φ-angle of helical ribs.
- H-height of ribs cross-sections.

The measured data of the main parameters are shown in Table 2. In Table 2, widths of helical ribs cross-sections is equal to widths of hoop ribs cross-sections, namely $b_h = b_c$.

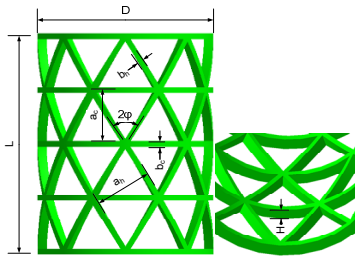

Fig. 1. Grid cylinder variables

3. Test and comparison

Test scheme should take structure features and loading conditions into consideration. Firstly, structure grippedends should be designed to avoid grippedends being destroyed in advance in loading. Secondly, load acting and load bearing should be improved to prevent local points or places of structures destroying in advance.

3.1. Compression test

The ends of the composite tube should be polished smoothly, clean, dry, to provide parallel and level face for compression test. Also, to ensure composite grid cylinder carrying compression load symmetrically, two ends of the composite grid cylinder are cured with epoxy resin. Compression test scheme are shown in Fig. 2.

The damage of composite tubes appears on the end of strcture. It is crushed (shown in Fig. 3).The damage of composite grid cylinder is complex in compression test. The nodes of composite grid cylinder, points at which ribs cross, appear delamination at first. After delamination, the load carrying capacity of ribs declines and the ribs begin buckling. Finally, with increase of compression load, delamination becomes more and more severe and some ribs break off (shown in Fig. 3).

In general, there are two main reasons that cause nodes of the composite grid cylinder delamination in advance.

- The nodes of the composite grid cylinder are points of rib intersections. The intersections cause fiber accumulation, bending and weaken strength and stiffness at nodes. So the nodes are

Table 2. Composite grid cylinder specimen parameter

Specimen	Quality (g)	L (mm)	Φ (°)	D (mm)	H (mm)	a_h (mm)	a_c (mm)	b_h=b_c (mm)
Compression	8.8	95	30	76.7	1.71	24.6	23.5	1.5
Bending	35.2	352	30	76.2	1.90	24.4	24.0	1.7
Torsion	31.5	350	30	77.3	1.61	25.2	24.5	1.7

the weakest place in the cylinder and they are damaged at first in compression test.

- During curing, composite grid cylinders are placed statically without rotating in high temperature stove. The resin flows into the lowest place in composite grid cylinder and cause some nodes resin loss.

The stiffness to weight ratio of the composite grid cylinder is about 45% of the composite tube. And the strength to weight ratio of the composite grid cylinder is about 19.4% of the composite tube. There are three main reasons weakening the strength/stiffness to weight ratio of the composite grid cylinder.

- Fiber volume fraction of composite grid-stiffened cylinder is low.
- Carbon fiber is damaged in wet winding.
- Fiber accumulation and resin loss weaken strength and stiffness of nodes.

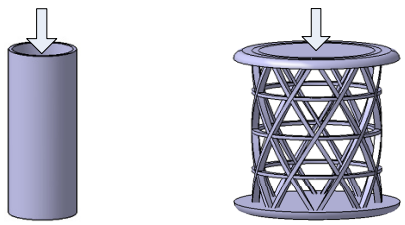

Fig. 2. Compression test scheme

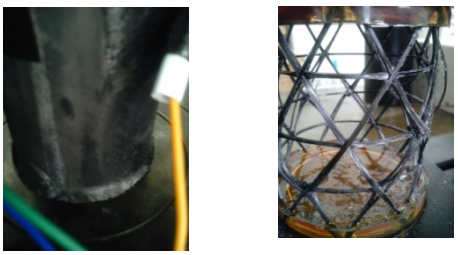

Fig. 3. Compression specimen damage

3.2. Torsion test

Composite tube grippedends are the weakest place in torsion testing and can be damaged easily by testing machine. To make matter worse, composite tube grippedends are so slipped that it is very hard to clamp them in load acting. In test preparation phase, to ensure the grippedends are enough burliness to avoid damaging in advance, composite tube grippedends are cured with resin inside and outside of composite tubes.

The ends of Composite grid cylinder can not carry clamping load from radial direction. In addition, the structure outer diameter is larger than inner diameter of testing machine grip. In test preparation phase, two ends of the composite grid cylinder are cured with resin to form grippedends. Torsion testing scheme are shown in Fig. 4.

The damage of composite tube is delamination of laminate in torsion testing (shown in Fig. 5). the damage of the composite grid cylinder also appear at nodes at first. It is delamination of nodes. With increase of torsion load, some ribs are broken off. Causes of nodes delamination are the same as in compression testing.

Torsion strength to weight ratio of the composite grid cylinder is about 31% of composite tube. Reasons which weaken torsion strength to weight ratio of the composite grid cylinder are the same as above mentioned in compression testing.

Fig. 4. Torsion test scheme

Fig. 5. Torsion specimen damage

3.3. Bending test

Three point bending test was not adopted to analyze bending resistance by material testing machine. Because the test specimens are cylinders and tubes, loading area is so small that it is easy to cause local failure in three point bending test. It is worse that support area, between test specimens and test equipments, is too small to finish three point bending test. In three point bending test, a

Table 3. Compressive property comparison

Specimen	Quality (g)	Stiffness (KN/mm)	Stiffness to weight ratio (KN/mm)/kg)	Ultimate load (KN)	Strength to weight ratio (KN/kg)
Tube	39.4	86.92	2206.09	73.58	1867.51
Grid cylinder	8.8	8.74	993.18	3.19	362.50

simple test device is adopted to measure structure stiffness. In the test scheme, two ends of specimens are cured with resin to form support ends. And weight is up in the middle of specimens, as loading. Deflection is measured by dialgage. The bending test scheme are shown in Fig. 6.

The stiffness to weight ratio of composite grid cylinder is about 2.7 times of the composite tube (shown in Table 5). When grid cylinder quality is the same as tube, grid cylinder can provide bigger outer diameter than tube. The composite grid cylinder with bigger outer diameter, have more second axial moment of area to improve bending stiffness.

Table 4. Torsional property comparison

Specimen	Quality (g)	Ultimate torque (kg·m)	Strength to weight ratio (kg·m/kg)
Tube	145.6	110.0	755.49
Grid cylinder	31.5	7.55	239.68

Fig. 6. Bending test scheme

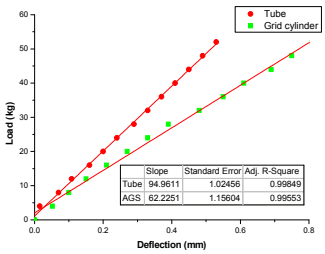

Fig. 7. Load vs. deflection

Table 5. Bending property comparison

Specimen	Quality (g)	Stiffness (kg/mm)	Stiffness to weight ratio ((kg/mm)/kg)
Tube	149.2	94.96	636.46
Grid cylinder	35.2	62.22	1767.61

4. Conclusions

The present work has provided effective reference for selection of structures, especially ultra-lightweight structure. Some conclusions, based on fabricating process and test scheme mentioned above, are in the following.

- Compression strength/stiffness to weight of grid cylinder is lower than tube; torsion strength to weight of grid cylinder is lower than tube; bending stiffness to weight of grid cylinder is higher than tube.
- Because of fiber accumulation, bending and resin loss,the joint, points of ribs intersections, is the weakest place in composite grid cylinder.
- Volume fraction, fiber damage in wet winding and fiber accumulation and resin loss at nodes, weaken strength and stiffness of the composite grid cylinder.

Refenrences

[1] V. V. Vasiliev, V. A. Barynin, A. F. Rasin, Anisogrid lattice structures-survey of development and application[J], Composite Structures 2001 54: 361-370

[2] Yu. O. Bakhvalov, V. P. Molochev, S. A. Petrokovskii, Proton-M Composite interstage structures: design, manufacturing and performance European conference for aerospace sciences (EUCASS)

[3] V. V. Vasiliev, A. F. Razin, Anisogrid composite lattice structures for spacecraft and aircraft applications[J], Composite Structures 2006 76: 182-189

[4] V. V. Vasiliev, V. A. Barynin, A. F. Razin. Anisogrid composite lattice structures-Development and aerospace applications [J], Composite Structures, 2012 94: 1117-1127

[5] Wegner, P.M., Ganley, J.M., Huybrechts, S.M., and Meink, T.E., "Advanced Grid Stiffened Composite Payload Shroud for the OSP Launch Vehicle", 2000 IEEE Aerospace Conference Proceedings.

[6] Peter M. Wegner, John E. Higgins, Barry P. VanWest, Application of Advanced grid-stiffened structures technology to the minotaur payload fairing, AIAA 2002-1336

[7] G. Frulla, E. Cestino, Design, manufacturing and testing of a HALE-UAV structural demonstrator[J], Composite Structures, 2008, 83: 143-153

[8] Giulio Romeo, Giacomo Frulla, Enrico Cestino, and Guido Corsino, HELIPLAT: Design, Aerodynamic, Structural Analysis of Long-Endurance Solar-Powered Stratospheric Platform[J], Journal of Aircraft 2004, 41(6).

Thermal laser micro-adjustment using ultra-short pulses

J. Griffiths, S. P. Edwardson, G. Dearden and K. G. Watkins
Laser Engineering Group, School of Engineering, University of Liverpool, Liverpool, L69 3GH, United Kingdom

Abstract. MEMS manufacturing requires accurate positioning and high reproducibility. Lasers can be utilised in accurate post-fabrication adjustment, allowing for manufacturing processes with relatively large tolerances. Laser micro forming (LμF) is a process for the precision adjustment, shaping or correction of distortion in micro-scale metallic components through the application of laser irradiation without the need for permanent dies or tools. The non-contact nature of the process is also useful in accessing specific micro-components within a device which may be highly sensitive to mechanical force. As such it has potential for widespread application in both the manufacturing and microelectronics industry. In this work, the micro-adjustment of 1000x300μm stainless steel actuator arms using a mode locked fibre laser with a maximum pulse energy and duration of 3 μJ and 20 ps respectively was conducted. The effect of pulse overlap, laser power, irradiation strategy and number of irradiations on the net bend angle is presented.In addition, the mechanism of thermal deformation is investigated through numerical modeling and the potential for its application in the micro-adjustment of MEMS scale components is discussed.

Keywords: Micro-adjustment, Laser Forming, Temperature Gradient Mechanism (TGM), MEMS, FEM

1. Introduction

Micro-electronic systems often comprise functional components which require highly accurate micro-scale adjustment after fabrication [1]. Such functional components are typically difficult to access and highly sensitive to mechanical force. The application of lasers offers the potential for controlled and repeatable micro-adjustment of these components in a contact free process.

At the macro-scale the LF process involves generating thermal stresses within a substrate using a defocused beam. Depending on the desired effect, the process parameters can be altered to either induce elastic-plastic buckling or plastic compressive strains. The most commonly employed mechanism is the Temperature Gradient Mechanism (TGM), which bends the sheet metal out of plane towards the beam. A steep thermal gradient is generated locally along the irradiation path, inducing more thermal expansion on the upper surface of the substrate. Upon cooling, providing the temperature was raised enough to cause sufficient thermal strain, plastic contraction occurs in this upper surface, creating a bend angle of 1-2^{o} per pass [2, 3].

When scaling down the LF process, limits to conventional thermal forming techniques become evident, such as excessive, non-localised heating of the substrate and long thermal relaxation times [4]. Research has been conducted on non thermal LμF techniques, such as utilising shockwaves generated through the breakdown of air to induce compressive stresses in the workpiece upper surface [5, 6]. Providing the fluence (Φ) is below or close to the ablation threshold (Φ_{th}) of the material, ultra-short pulses have the potential to be used to form materials in a thermal process. When the pulse duration is shorter than the lattice interaction time, as is often the case with sub nanosecond pulses, there is little conductive heat transfer into the bulk material. This confines the heating effect to the surface layer of the material, thereby selectively inducing plastic compressive stresses and avoiding thermal damage of the substrate, as investigated in this paper.

2. Experimental

2.1. Design and manufacture of micro-scale actuators

The investigation initially consisted of the design of a suitable micro-scale component and selection of an appropriate laser source for their manufacture. 1000x300μm MEMS scale actuator-style arms (Fig 1) were designed and micromachined out of 50 and 75μm thick AISI 302 stainless steel sheet (Table 1).

The microactuators were fabricated using a High-Q IC-355-800nm, 50 kHz laser operating at 1064nm. The laser parameters used were 5 kHz repetition rate, 300mW average power, 50mm/s traverse speed, 10ps pulse length and a 35μm spot diameter. 600 irradiations were required to penetrate the material thickness.

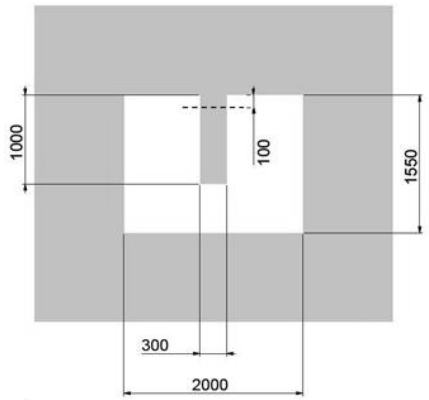

Fig. 1. Schematic of stainless steel AISI 302 actuator style arms, with dimensions in µm

2.2. Laser forming actuators

An experimental study of LµF was conducted using a 3W Fianium Yb-doped fibre TEM_{00} laser with a pulse length of 20ps, operating at 1059-1069nm and 500kHz. using a Veeco NT1100 white light interferometer to measure the resulting bend angle. The study comprised of adjusting the height of the actuator arms at various fluences and numbers of irradiations. The irradiation path was 100µm from the base of the actuator arm.

2.3 Numerical modelling

To fully understand the thermal aspects of the LF process an FE model was developed. A 2005 element thermal simulation of the laser forming of 300x1000x50µm AISI 302 stainless steel was developed using COMSOL MultiPhysics version 3.5a (Fig 2).

The governing equation for conduction in a solid is the Fourier heat equation (Equation 1).

$$\rho C_p \frac{\partial T}{\partial t} = \nabla.(k\nabla T) \tag{1}$$

Where is the density (kg/m^3), Cp is the specific heat capacity (J/kgK), T is the temperature (K), t is the time (s) and k is the thermal conductivity (W/mK). The term ∇ is the differential or gradient operator (sometimes referred to as the Nabla operator) for three dimensional Cartesian co-ordinate systems. With the exception of the irradiated area the heat flux (q) at a given boundary is governed by Equation 2.

$$-n.q = -n(-k\nabla T) = q_0 + h(T_{\inf} - T) + \varepsilon\sigma(T_{amb}^4 - T^4) \tag{2}$$

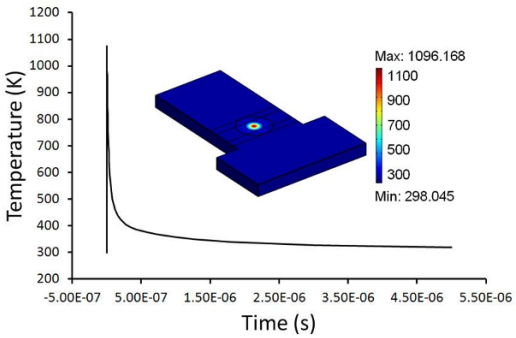

Fig. 2. Comsol MultiPhysics FE model output for the top surface directly on the laser scan line [1000x300x50µm stainless steel AISI 302, 35µm beam diameter, 500kHz repetition rate, 10mm/s traverse speed]

Where h is the heat transfer co-efficient (25 W/m^{2}K) and T_{amb} is the ambient temperature (298.15 K). The incident laser beam was approximated by a Gaussian distributed heat source (Equation 3) with a temperature dependant absorption coefficient [7].

$$I = I_0 e^{-\left(-\frac{2r^2}{\omega_0^2}\right)} = \frac{2E_p}{L_p \pi r^2} e^{-\left(-\frac{2r^2}{\omega_0^2}\right)} \tag{3}$$

Where E_p is the laser pulse energy (J), L_p is the pulse duration, r is radial distance (m) and ω_0 is the beam radius. The heat source was pulsed through the use of an interpolation function, consisting of a time-dependant Gaussian distributed pulse shape, repeated at regular intervals determined by the repetition rate of the laser.

Material properties were sourced from the ASM Metals Handbook and COMSOL's built in materials library. Thermal expansion coefficient (α_{th}), specific heat capacity (C_p), thermal conductivity (k) and density (ρ) were all considered temperature dependant.

The actual geometrical dimensions of the actuator were truncated to leave only the region of interest around the irradiation path. The mesh density was highest along the irradiation path, 100µm from the base of the actuator arm, with the maximum element size being 2.5e^{-6}m. A higher mesh density was assigned to the region of most interest at the centre of the irradiation path where most measurements were taken, where the maximum element size was restricted to 1e^{-5}m (Fig 3).

Table 1. AISI 302 material properties at 298.15K. * Denotes properties considered temperature dependant in numerical simulations

α_{th}^* [1/K]	C_p^* [J/kg.K]	E [Pa]	h [W/m^{2}K]	k* [W/m.K]	ρ^* [kg/m^3]	σ_{ys} [Pa]	v [1]
17.2e^{-6}	500	1.93e^{11}	25	16.2	8000	2.05e^8	0.27

3. Results

3.1. Ablation threshold determination

Prior to thermal LμF being conducted the ablation threshold fluence (Φ_{th}) of the stainless steel substrate was determined experimentally [9] using a 3W Fianium Yb-doped fibre TEM_{00} laser with a pulse length of 20ps, operating at 1059-1069nm and 200kHz. The average power was varied in 50 mW intervals from 100 to 650 mW, with 12 holes drilled at each power. Due to the dependence of Φ_{th} on number of pulses per spot [10] the experiment was repeated for 400 and 600 pulses per drilled spot for validation purposes. The diameter (D) of the ablated craters was measured using a Veeco NT1100 white light interferometer.

The beam radius (ω_0) was determined from a plot of D^2 against E_p and found to be 14.7μm. Using this value the fluence could be determined, and the x-intercept of a logarithmic trend line from a plot of D^2 against Φ_0, plotted on a Log_{10} scale, was taken as Φ_{th}. This was found to be 0.1J/cm^2 and 0.06J/cm^2 for 400 and 600 pulses, respectively. Equation 4 describes the relationship between peak fluence (Φ_0) and E_p, whilst D is related to Φ_0 according to Equation 5.

$$\Phi_0 = \frac{2E_p}{\pi\omega_0^2} \tag{4}$$

$$D^2 = 2\omega_0 \ln\left[\frac{\Phi_0}{\Phi_{th}}\right] \tag{5}$$

3.2. LμF using Picosecond pulse durations

Multi-pass LμF was conducted using a 3W Fianium Yb-doped fibre TEM_{00} laser with a pulse length of 20ps and spot diameter of approximately 30μm, operating at 1059-1069nm. The irradiation path was 100μm from the base of the arms. Laser micro-adjustment was conducted using both 200 kHz and 500 kHz whilst keeping the pulse energy constant at 3μJ.

Figure 3 reveals little deformation at 200 kHz but significant deformation at 500 kHz, suggesting the latter is the more suitable repetition rate for the laser micro-adjustment process. This can be attributed to the relatively larger cumulative build up in temperature at higher repetition rates due to reduced dwell time between pulses (Fig 4).

Figure 4 reveals a larger cumulative increase in temperature over the same period of time at constant pulse energy for 500 kHz than for 200 kHz. This can be attributed to the shorter interval between pulses.

Operating at 500 kHz, and with increasing multiple irradiations, a cumulative increase in bend angle was observed, as shown in Fig 5.

In addition to a cumulative increase in bend angle, an ablated groove was also observed along the length of the scan path, the aspect ratio of which became too large to resolve the depth by using white light interferometry with multiple irradiations (Fig 6).

This ablated groove can be attributed to the use of multiple irradiations in conjunction with fluences above those of the experimentally determined values of Φ_{th}. An experiment was therefore conducted in which the traverse speed was increased and the ablated groove depth and bend angle was monitored (Fig 7).

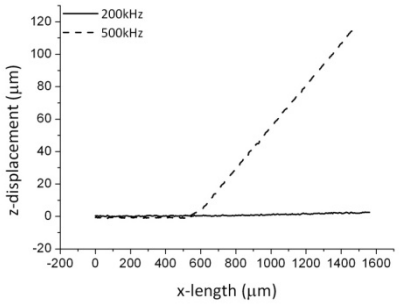

Fig. 3. Profile view of z-deformation after 10 irradiations at 200 and 500 kHz repetition rate and 3μJ pulse energy [1000x300x50μm stainless steel AISI 302, 35μm beam diameter, 10mm/s traverse speed]

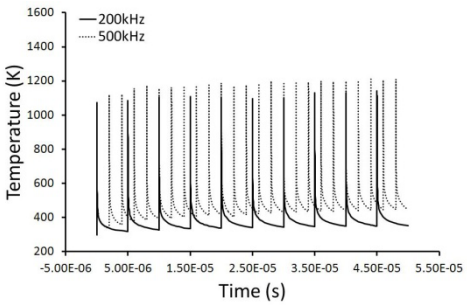

Fig. 4. FE simulation of temperature directly beneath the beam for a stationary laser heat source at 200kHz and 500kHz [1000x300x50μm stainless steel AISI 302, 3μJ pulse energy, 35μm beam diameter]

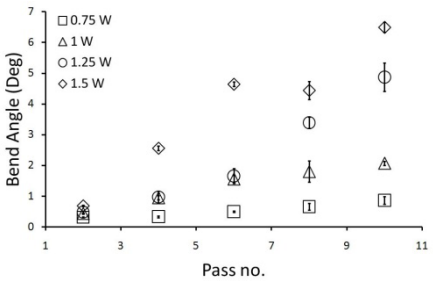

Fig. 5. Cumulative bend angle variation with successive irradiations [1000 x 300 x 50μm stainless steel AISI 302, 35μm beam diameter, 500kHz repetition rate, 10mm/s traverse speed]

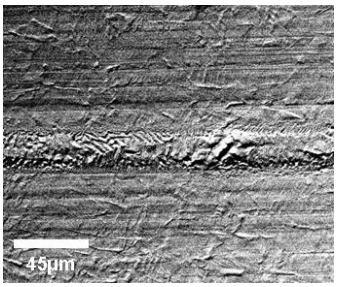

Fig. 6. Scanning electron microscope image of ablated groove after 1 scan [1000 x 300 x 50µm stainless steel AISI 302, 1500mW, 35µm beam diameter, 500kHz repetition rate, 10mm/s traverse speed]

From Fig 7 it is evident that the ablated groove has a detrimental effect on bend angle up to a point, in this instance when deeper than ~2µm. This detrimental effect can be attributed to the relatively large ablated groove depth when compared to the thickness of the thin section steel sheet. The optimum traverse speed at which a suitable combination of bend angle z-depth was achieved was found to be 35mm/s.

Whilst it was possible to limit the ablation depth for single scans, multiple irradiations caused the ablation depth to increase in an exponential fashion. This phenomenon could be attributed to a conditioning of the irradiated surface after an initial irradiation [9], increasing the absorption for subsequent scans. As such an alternative method to multiple irradiations was required to obtain a variation in bend angle. One such method investigated involved a combination of varying power and a hatched scan strategy. The hatch consisted of four single irradiation paths, scanned sequentially in alternate directions, each 30µm apart allowing for little or no overlap (Fig 8).

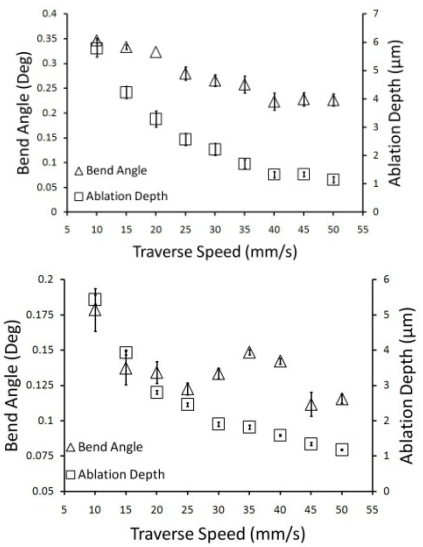

Fig. 7. Bend angle and ablation depth variation with increasing speed, 50 and 75µm thickness left and right respectively. [1000x300µm stainless steel AISI 302, 35µm beam diameter, 500kHz repetition rate, 1.5W average power]

Through variation of laser power with a single line scan strategy, controlled and repeatable micro-adjustment was achieved. The application of a hatched scan strategy increased the range over which micro-adjustment could be achieved whilst keeping the ablated groove to within~2µm depth (Fig 9).

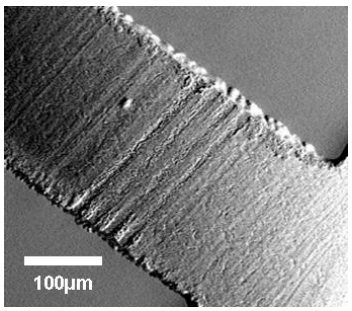

Fig. 8. Scanning electron microscope image of ablated groove after hatch irradiation strategy [1000 x 300 x 50µm stainless steel AISI 302, 1500mW, 35µm beam diameter, 500kHz repetition rate, 35mm/s traverse speed]

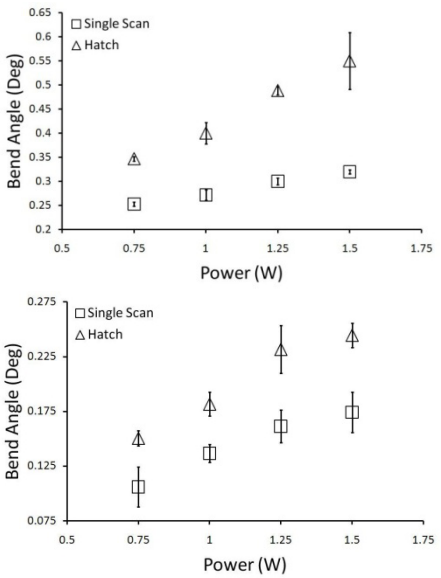

Fig. 9. Bend angle variation with increasing power, 50 and 75µm thickness top and bottom respectively. [1000 x 300µm stainless steel AISI 302, 35µm beam diameter, 500kHz repetition rate, 35mm/s traverse speed]

4. Conclusions

This investigation has demonstrated thin sheet LµF for the micro-adjustment of actuator style components conducted using picosecond duration pulses, with no absorptive or tamping layers required. This novel technique combines short pulse durations with high repetition rates and offers a method of generating localised heat build-up on the top surface of micro-scale

components, allowing for controlled and repeatable micro-adjustment. Through a combination of irradiation strategies a large range of deformation is achievable. Empirical and numerical studies were conducted, with an emphasis on the use picosecond pulse durations in LμF. The pulse duration must be sufficiently short as to limit the heat diffusion depth to within a suitable range (i.e. half the sheet thickness) yet not so short that the intensity causes significant material removal. Additionally the repetition rate or degree of pulse overlap must be high enough to ensure a build up in temperature on the surface of the component suitable for thermal forming. The process has significant potential for the post-fabrication micro-adjustment of functional components in micro-electronic devices. Challenges include minimising ablation along the irradiated scan path and obtaining a larger range of deformation through optimised process parameters.

References

[1] G. Dearden, S. P. Edwardson, Some recent developments in two- and three-dimensional laser forming for ‘macro’ and ‘micro’ applications, J. Opt. A: Pure Appl. Opt. 5 (2003) 8–15

[2] M. Geiger and F. Vollertsen, The Mechanisms of Laser Forming, CIRP ANNALS 42 (1993), pp. 301–304

[3] J. Magee, K. G. Watkins, W. M. Steen, Advances in Laser Forming, J. Laser Appl. 10, 235 (1998)

[4] M. Dirscherl, G. Esser, M. Schmidt, Ultrashort Pulse Laser Bending, JLMN- Journal of Laser Micro/Nanoengineering, Vol. 1, No. 1, 2006

[5] J. Zhou, Y. Zhang, X. Zhang, C. Yang, H. Liu, J. Yang, The Mechanism and Experimental Study on Laser Peen Forming of Sheet Metal, Key Engineering Materials Vol. 315-316 (2006) pp607 611

[6] Kenneth R. Edwards Stuart P. Edwardson Chris Carey Geoff Dearden Ken G. Watkins, Laser Micro Peen Forming Without a Tamping Layer, Int J Adv Manuf Technol (2009)

[7] T. J. Wieting, J. L. DeRosa, Effects of surface condition on the infrared absorptivity of 304 stainless steel, J. Appl. Phys. 50(2), February 1979

[8] P. Mannion, J Magee, E. Coyne, G. O’Conner, Ablation thresholds in ultrafast micro-machining if common metals in air, Proc. Of SPIE, Vol. 4876 (2003)

[9] P. Mannion, J. Magee, E. Coyne, G. O’Connor, T. Glynn, The effect of damage accumulation behaviour on ablation thresholds and damage morphology in ultrafast laser micro-machining of common metals in air, Applied Surface Science 233 (2004) 275–287.

Precision mould manufacturing for polymer optics

M. Speich[1], R. Börret[1], A.K.M. DeSilva[2] and D.K. Harrison[2]
[1] Aalen University, Aalen, Germany
[2] Glasgow Caledonian University, Glasgow, UK

Abstract. Ophthalmic lenses, sensors and sunglasses, for example, are commonly made of polymer materials. Therefore polymer optics is a growing market mainly for medium quality optics but also for precision optics. Polymer optics are usually produced in an injection moulding process. Due to high quality requirements on the final product the manufacturing process of the moulds has to be very accurate and precise. Thus the master tool has to be fabricated to a high quality with regard to shape accuracy and roughness. The focus of this paper is on the process chain for the fabrication of moulds for polymer optics. The typical existing process chains contain steps like to nickel plating, diamond machining and manual polishing. Some of these steps are expensive and require very experienced Staff. In the new process chain an industrial robot with special tools is used for lapping and polishing. Robot polishing replaces the former nickel plating, diamond machining and manual polishing steps. The lapping / polishing process was newly developed to achieve appropriate results. Different tool materials, polishing agents and process parameters have been tested to obtain excellent results directly on hardened steel moulds. Aalen University and UVEX ARBEITSSCHUTZ GMBH have started this project together with Saarland University Faculty of Medicine. The goal of this work is to achieve a ready to use steel mould with a roughness better than 5nm rms and an overall shape accuracy better than 4µm; with just one process step after grinding.

Keywords: robot polishing, mould manufacturing, mould fabrication, precision polishing

1. Introduction

This work focuses on the manufacturing of steel moulds for polymer optics. Polymer optics is a growing market. Applications using polymer optics can be found in almost every area of daily life moreover they are of fundamental use for military issues and medical applications f.e. [1].

Polymer injected optics are usually produced in high numbers. From low cost products with several million polymer parts per mould up to precision optics with quantities of some hundreds the demands on the moulds are very similar [2].

The topic of this work arose out of a research project with UVEX ARBEITSSCHUTZ GMBH. UVEX, a producer of safety goggles, is also using plastic injection moulding for their optics. Moulds are of different sizes and the radius of curvature also varies. UVEX also uses this process to produce plastic visors for helmets. So there is need of spherical as well as of cylindrical moulds. Another problem is that wearers or workers who are supposed to wear safety goggles often criticize the image quality of the goggles. Fig. 1. shows a barcode seen through goggles in accordance to DIN standards [3].

Fig. 1. left: image definition without safety glasses; right: image definition with safety glasses conform to DIN EN 166 (simulation)

1.1. Present process chain

Present process chains for mould manufacturing usually consist of 5 steps. These 5 steps can be seen in the following Fig. 2.

The first step is to shape the work piece, therefore usually milling or grinding machines are used. The goal of this first step is to get the best possible surface with a high rate of material removal. [4-6] All following processes have to deal with the results of the first material removal and sometimes structures from grinding remain on the surface until the last polishing. So the surface roughness should be already really good after this first process step. [7]

After grinding, the steel mould is usually nickel plated. Nickel plating can lead to lifetime issues because the surface can get small cracks after some hundred injection runs. So it would be interesting to avoid this step. But this step is necessary to enable the third process step, diamond machining. Normally diamond machining cannot be used for steel parts but there are several attempts to avoid nickel plating and use diamond machining directly on steel surfaces. [8] Usually diamond machining is used to bring the nickel plated surface to a

good shape and to produce good roughness values. Not forgetting diamond machining is a rather expensive process, the purchase of diamond machining equipment and machines are almost impossible for small and medium sized enterprises.

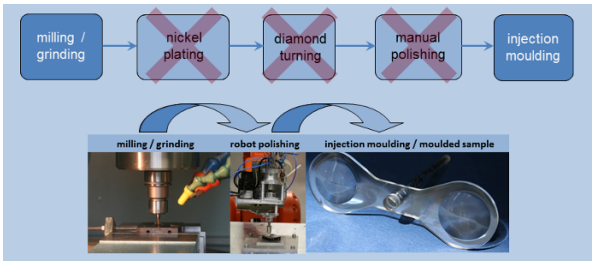

Fig. 2. Present vs. new process chain; 3 instead of 5 steps

After diamond machining the mould is normally manually polished. Manually polishing is a very labour intensive and experience requiring process step. [9] Manual polishers have to be really experienced and skilled to polish steel moulds in specifications for polymer optics. The moulds are not supposed to show any visible defects to achieve good results on polymer parts.

1.2. New process chain

The goal of this work is to find a new process chain that is also feasible for small and medium enterprises. Therefore expensive and difficult to handle process steps are to be superseded with an easy to handle cheap and stable process step. This can be seen in Fig. 2, robot lapping / polishing is used instead of nickel plating, diamond machining and manual polishing. One big advantage of the usage of an industrial robot is independence on machine restrictions. As long as the mould is in the working range of the robot it can be worked with the new process.

One robot step will not be sufficient to achieve the desired results starting from a ground sample. To obtain real results the sample material was chosen according to current mould steels. The steel used for first experiments have been hardened to approx. 59 HRC before grinding. [10]

2. Process development

Process development was started on plane steel samples to determine the best working tool material and polishing agent. The robot moved the steel sample in a constrained movement on the tool. The hardness of the tools was varied for different working steps; first lapping was done with hard tools and then the tool grew softer with every step. For polishing soft tools of polyurethane were chosen.

There have been some experiments to determine an appropriate polishing agent. Different kinds of diamond powder in all sorts of grain sizes have been investigated; starting with cheap monocrystalline diamond powder up to expensive polycrystalline powders. In first tests the cheap, edgeless diamond powder led to pores and pitting on the surface. Pitting is an undesirable defect; carbides are pulled-out of the steel matrix by diamond grain as can be seen in Fig. [11].

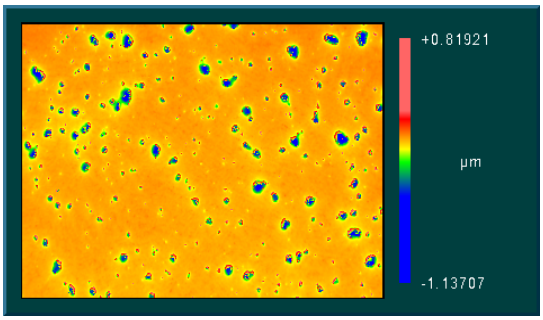

Fig. 3. Pitting after 2 polishing steps
(field of view 4.94 x 3.70 mm, PV 1956 nm, rms 80 nm)

Synthetic diamond turned out to be an appropriate polisihing agent that leads to good material removal rates on hardened steel samples.

With this polishing agent different tool materials have been investigated. Tests showed that hard tools lead to high material removal rates with a big diamond grain size; softer tools lead to better roughness values but the material removal rate was substantial smaller.

The first experiments for process development were realised on plane samples with large, plane tools. To work on spherical or cylindrical moulds or even on freeform shaped moulds it is necessary to develop a process with small tools with different radii of curvature. Therefore the knowledge gained in the experiments with large tools and plane samples was transferred to small tools and different mould shapes.

Fig. 4 shows a polishing head that was developed in Aalen University.

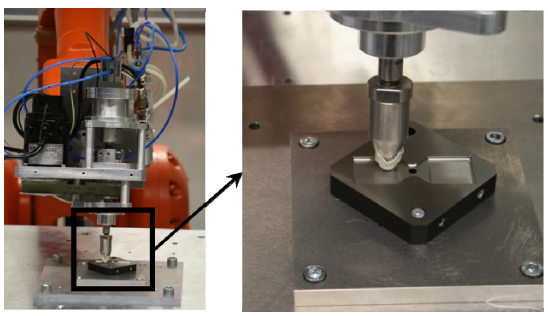

Fig. 4 left: Industrial robot with polishing head, right: Tool with soft cloth [12]

The polishing head rotates the tool and generates the pressure on the surface and is fixed to the industrial robot. The movement on the surface is performed by the industrial robot. The robot movement is generated with an offline programming tool that allows different robot tool paths.

2.1. Tool path

After an appropriate combination of tool and polishing agent was found the influence of the working tool path was investigated. Usually the experiments have been done with linear tool paths and two working directions. But the results showed that the tool footprint is not symmetrical, this is why the tool path was specially investigated. Fig. 5 shows the results after a polishing step with linear tool path and two working directions. It is clearly visible that the tool path is directly reproduced on the surface; this leads to a rough structure on the surface with a PV of 97 nm which is not required.

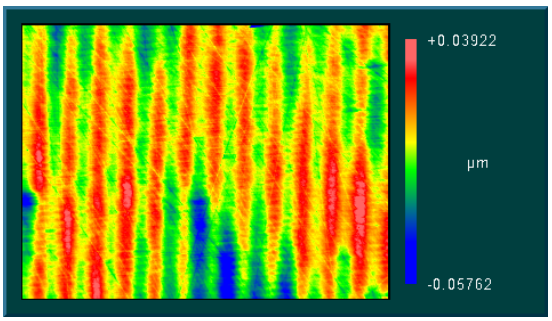

Fig. 5. Tool path visible after polishing in both meander directions (field of view 4.94 x 3.70 mm, PV 97 nm, rms 14 nm)

To remove these structures the tool path was changed and the surface was just worked in one direction. The robot movement was the same as before but the tool was not in contact with the surface on its way back. Fig. 6 shows that there is a substantial difference between polishing in both linear directions or just in one linear direction. Several other tool paths have already been investigated. [13]. Later samples have always been polished either in just one linear direction or with spiral tool path. Especially spherical moulds are often polished like this, due to rotational symmetry. The CNC code for the robot control has been generated in proprietary software from the Centre of Optical Technologies of Aalen University.

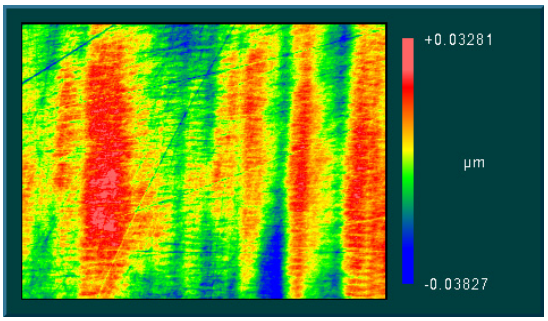

Fig. 6. Surface more homogenous with just one working direction (field of view 4.94 x 3.70 mm, PV 71 nm, rms 10 nm)

3. Conclusions

The results so far show, that the new process chain can be used to polish moulds to a ready to use state for standard moulds. Depending on tool material and mould material several steps are necessary to achieve good surfaces free of visible defects. The number of required lapping and polihsing steps is also heavily dependent on the state of the mould after grinding. The polishing agent has to be adapted to the tool material. But roughness values of rms 10nm can be obtained very steadily with different combinations of polishing agent, tool material and other process parameters. So the process is very stable.

4. Outlook

Up to now it is not certain if the polished moulds are good enough for the production of polymer optics. This will be evaluated in injection moulding tests.
Furthermore the contact area between the tool and the mould surface will be simulated with finite element method. The results of these simulations are inteded to help in characterising new materials with different surface layer properties to select an appropriate tool footprint. Furthermore the finite element analysis should help to understand the problems with the toolpath visible after polishing. The material removal is to be simulated with this new approach. Results will be used for trajectory planning of totally new tool paths.

Acknowledgments: The authors would like to thank the Bavarian Research Foundation for funding IVOS research project.

References

[1] Beich, W.S., (2002) Plastic Optics - Specifying Injection-Molded Plastic Optics. Photonics Spectra, 2002. 36(3): 127-132.

[2] Hering, E. and Martin, R., Fertigung optischer Komponenten und Systeme (Manufacturing of optical components and systems), in Photonik - Grundlagen, Technologie und

Anwendung (Photonics - Basics, technology and application), 2005, Springer: Berlin. 105-128.
[3] Speich, M. and Börret, R., (2011) Mould fabrication for polymer optics. Journal of the European Optical Society: Rapid Publications, 2011. 6.
[4] Brinksmeier, E., Mutlugünes, Y., Klocke, F., Aurich, J.C., Shore, P., and Ohmori, H., (2010) Ultra-precision grinding. CIRP Annals - Manufacturing Technology, 2010. 59(2): 652-671.
[5] Comley, P., Walton, I., Jin, T., and Stephenson, D.J., (2006) A High Material Removal Rate Grinding Process for the Production of Automotive Crankshafts. CIRP Annals - Manufacturing Technology, 2006. 55(1): 347-350.
[6] Mandina, M.P., Design, Fabrication, and Testing; Sources and Detectors; Radiometry and Photometry, M. Bass, Editor 2009.
[7] Rebeggiani, S. and Rosén, B.-G., High gloss polishing of tool steels – step by step, in Proceedings of The 4th International Swedish Production Symposium2011. p. 257-262.
[8] Dong, J., Glabe, R., Mehner, A., Brinksmeier, E., and Mayr, P., Method for micromachining metallic materials, 2006.
[9] Altan, T., Lilly, B., and Yen, Y., (2001) Manufacturing of Dies and Molds. CIRP Annals - Manufacturing Technology, 2001. 50(2): 404-422.
[10] Rockwell, S.P., Hardness Testing Machine, U.S.P. Office, Editor 1924.
[11] Klocke, F., Rosén, B.-G., Behrens, B., Rebeggiani, S., and Zunke, R., Towards robust polishing strategies for moulds and dies, in Proceedings of the 3rd Swedish Production Symposium, Göteborg, Sweden, 2-3 December 2009 (SPS09)2009, Swedish Production Academy.
[12] Börret, R., Klingenmaier, J., Berger, U., and Frick, A., (2008) Minimized process chain for polymer optics. Proceedings of SPIE 2008. 7061(Novel Optical Systems Design and Optimization XI): 706118-706118-8.
[13] Tam, H.-y. and Cheng, H., (2010) An investigation of the effects of the tool path on the removal of material in polishing. Journal of Materials Processing Technology, 2010. 210(5): 807-818

Gradient vector method for computing feed-paths and hot-spots during casting solidification

M. Sutaria and B. Ravi
Mechanical Engineering Department, Indian Institute of Technology Bombay, Powai, Mumbai, India

Abstract. In this work, we present a computationally efficient approach to visualise 3D feed-paths and identify hot-spots inside a solidifying metal casting. The proposed Gradient Vector Method (GVM) involves computing the interfacial heat flux vector using an analytically derived solution to the heat transport equation, assuming virtual adjunct of material equivalent to metal-mould interface resistance. The casting geometry is divided into a finite number of radial segments and the resultant flux vector indicates the direction of the highest temperature gradient, which is normal to liquid-solid interface. The feed-path is computed by continuously tracking the successive approximate solutions. The GVM is found to be an order of magnitude faster than Level-set and other numerical methods for casting simulation. Its capability in identifying multiple hot-spots has been validated by casting experiments. Owing to its accuracy and speed, GVM is better suited to optimizing the feeding systems of castings, compared to conventional simulation methods.

Keywords: Casting, feed-path, hot-spot, shrinkage, simulation, solidification.

1. Introduction

During casting solidification and resultant volumetric contraction, hotter metal from adjacent locations flows to the solidifying region along 'feed-paths'. The feed-paths propagate along the maximum temperature gradients, and converge at the last solidifying points, the 'hot-spots'. These are the most probable locations for defects such as shrinkage cavity, porosity, and centre-line shrinkage as shown in Fig. 1(a), (b), and (c). These defects can be minimized by designing an appropriate feeding system to ensure directional solidification from thin to thick sections in the casting, finally leading to feeders.

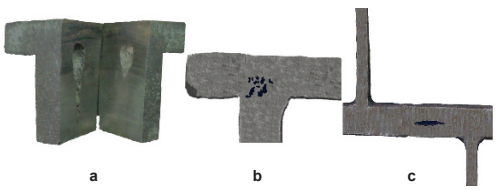

Fig. 1. Shrinkage. a. concentrated; b. distributed; c. centre-line

Over the years, a considerable amount of experimental, analytical, and numerical work has been carried out to understand casting solidification and feeding mechanism. Early experimental work to estimate the feeding distance during solidification was carried out by Myskowski et al. [1]. The feeding guidelines are empirical in nature and do not account for boundary conditions. This limitation can be overcome by the use of analytical solutions of casting solidification. Most of the early analytical work was carried out based on variants of Neumann [2] solution. Garcia et al. [3] proposed and discussed virtual adjunct method to account for resistance at metal-mould interface. Analytical solutions are however, limited to unidirectional and axisymmetrical solidification problems.

More generalised solutions use numerical methods involving finite approximation to the solution of the governing equations. The enthalpy method [4], volume of fluid method [5] and level-set-method [6] are some of the most widely used physics-driven methods to compute temperature and solid fraction during solidification. Sutaria et al. [7] proposed level-set-method for feed-path and hot-spot computation using combined Eulerian-Lagrangian framework. All these methods are based on manipulation of huge matrices and iterative calculations, making them computationally intensive [8]. Ravi and Srinivasan [9] proposed a computationally efficient geometry-driven approach called Modulus Vector Method (MVM), using geometric modulus (ratio of volume to heat transfer area) to compute feed-paths.

From the literature, four major conclusions can be drawn. First, feeding distance rules in general do not account for complex geometries, as well as variation in material properties and boundary conditions. Second, analytical solutions are applicable to only simple unidirectional and axisymmetric problems and are of limited use in practice. Third, numerical techniques can overcome above limitations and are versatile, but require accurate values of material properties and boundary conditions and are computation intensive. Fourth, the MVM takes less computation time but is essentially a

geometry-based technique and appears to lack in the accuracy of feed-path profile, especially near the metal-mould boundary. The aim of the present work is to evolve an improved method to compute hot-spots and feed-paths, suited to automatic evaluation and optimization of feeding systems. The accuracy of the proposed method is benchmarked with MVM as well as level-set-method.

2. Gradient Vector Method (GVM)

A casting solidifies progressively from the mould boundary until it converges to last solidifying points in the mould-cavity, known as hot-spots. Feeding at any given point (compensation for volumetric contraction) occurs in the direction of the highest temperature gradient along the liquid-solid interface.

2.1. Interfacial heat flux

The principle of the proposed GVM is illustrated with a control volume (Fig. 2). Consider a point P_i on liquid-solid interface at time τ. The control volume is divided into n radial segments from P_i. Taking infinitesimally small segment angle, the interfacial heat flux due to evolution of latent heat in radial segment s is given by:

$$q_s = \rho_c L\left(\partial r/\partial \tau\right) \tag{1}$$

where, ρ_c is density of cast metal, L is latent heat evolved, and $\partial r/\partial\tau$ represents liquid-solid interface velocity (solidification velocity). The expression for interfacial velocity is derived based on following assumptions:

- The heat flow is unidirectional in each segment, along the radial direction.
- The heat transfer coefficient at metal-mould interface remains constant during solidification.
- Temperature diffusivity of the metal and mould material is independent of the temperature.

Solidification time is computed for each segment by adding a virtual layer of solid metal and mould as suggested by Garcia et al. [3]. The basic notion involves consideration of interface resistance as equivalent to pre-existing adjunct of material. The thermal contact between metal and mould is then assumed perfect and represented by an infinite heat transfer coefficient. The expression for solidification time is:

$$\tau_{sol} = \frac{1}{4\varphi^2\alpha}\left(\frac{r}{2}\right)^2 + \frac{k_c}{hSt\alpha}\left(\frac{r}{2}\right) \tag{2}$$

where, r is average radius of segment, φ is solidification constant, k_c is thermal conductivity of the metal, α is thermal diffusivity of cast metal, h is heat transfer coefficient at metal-mould interface and St is Stefan number.

$$St = C_c\left(T_f - T_m\right)\Big/L$$

where, T_f is freezing temperature of the metal, T_m is mould temperature, and C_c is specific heat of cast metal.

Solidification constant φ is computed by deriving thermal balance at liquid-solid interface [Eq. (3)].

$$\sqrt{\pi}\varphi e^{\varphi^2}\left(Dt + erf\left(\varphi\right)\right) = St \tag{3}$$

where, $Dt = \sqrt{k_c\rho_c C_c/k_m\rho_m C_m}$. Here, ρ_m, k_m, and C_m are density, thermal conductivity, and specific heat of mould material, respectively.

Interface (solidification) velocity is computed by differentiating Eq. (2) with respect to r:

$$v_{sol} = \frac{\partial r}{\partial \tau} = \frac{8\varphi^2\alpha StBi}{r\left(StBi + 4\varphi^2\right)} \tag{4}$$

where, Biot number, $Bi = hr/k_c$. Interfacial heat flux for segment s is computed by substituting Eq.(4) into Eq.(1)

$$q_s = \rho_c L\frac{8\varphi^2\alpha StBi}{r\left(StBi + 4\varphi^2\right)} \tag{5}$$

The expression given by Eq. (5) shows that interfacial heat flux is a function of casting geometry, material properties and boundary conditions. At a hot-spot, the vector sum of these segmental interfacial heat fluxes is zero; here the liquid-solid interface vanishes, forming a singularity. If the vector sum is non-zero, the resultant vector indicates the direction of the highest temperature gradient, which is normal to liquid-solid interface profile. Interface movement occurs in the opposite direction as shown in Fig. 2. The resultant interfacial heat flux is directed outwards (solid phase) where as interfacial velocity vector is directed inwards (liquid phase).

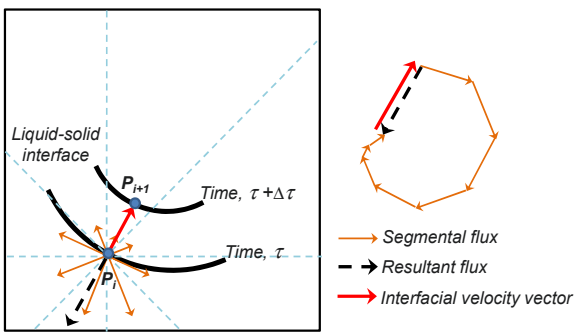

Fig. 2. Computation of interfacial heat flux and velocity vector

2.2. Computation of hot-spot and feed-path

Feed-path is computed by continuously tracking the direction of the resultant interfacial heat flux. The methodology is illustrated with a control volume as shown in Fig. 3. Let us assume that the hot-spot lies at position P_i on liquid-solid interface as an initial solution. Consider a mass-less particle lying at P_i and compute the direction of resultant interfacial heat flux by dividing the casting geometry into infinitesimal number of segment as explained in previous section. Direction of interfacial velocity vector and resultant interfacial heat flux will be opposite to each other as shown in Fig. 3. The mass-less particle is marched along the interfacial velocity vector direction with a small step Δs as shown by thin arrows in Fig. 3. The new position of mass-less particle is:

$$P_{i+1} = P_i + \vec{v}\Delta s \tag{6}$$

where, $\vec{v}$ is the unit vector along interfacial velocity.

The procedure is repeated at P_{i+1} and continued until it reaches a position where the solution converges (the resultant interfacial heat flux is negligible). This last position P_{i+m}, correspond to the point of local maxima of temperature, and represent the local hot-spot. During solidification, when temperature T_i of the molten metal at position P_i reaches the solidus temperature, the feed metal to compensate volumetric shrinkage is supplied from P_{i+1}, since it has the highest temperature gradient toward P_i. Thus feeding occurs in opposite direction to the mass-less particle movement, that is, from P_{i+m} to P_i as shown by thick solid arrow in Fig. 3.

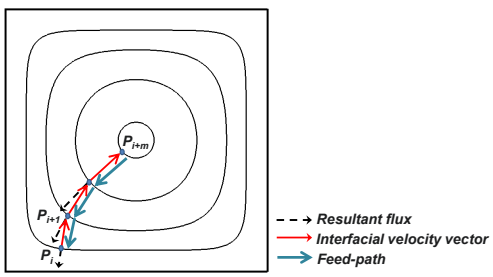

Fig. 3. Hot-spot and feed-path computation

3. Benchmarking and validation

Analysis of two sand castings has been carried out to demonstrate and evaluate the performance of GVM. The first one is a 4.5 Kg 'C' shaped cast steel (0.2% C) part with thickness 0.1 m. The second one is a 2.5 Kg multiple junction ductile iron (500/7) part with thickness 0.04 m. They have different geometric features like re-entrant corners and junctions. The feed-path and hot-spot results are compared with MVM [9] and benchmarked with result obtained by LSM [7]. Finally, validation is carried out by performing experiments.

3.2. Benchmarking with MVM and LSM

Propogation of feed-paths in the right and left arm of the 'C' shaped casting, computed using GVM, is shown in Fig. 4 (a). The GVM feed-paths starting from all part boundaries are shown in Fig. 4 (b). The feed-paths from the same starting points, computed using MVM, are shown in Fig. 5 (a). The GVM feed-paths are (correctly) normal to the part boundary, whereas MVM feed-paths are slightly inclined. The GVM (corretly) exhibits a series of hot-spots, whereas MVM exhibits a single hot-spot in the right bottom junction. The feed-paths computed using LSM are shown in Fig. 5 (b). The direction of the feed-paths as well as their convergence points (hot-spots) obtained by LSM are in close agreement with those obtained from GVM.

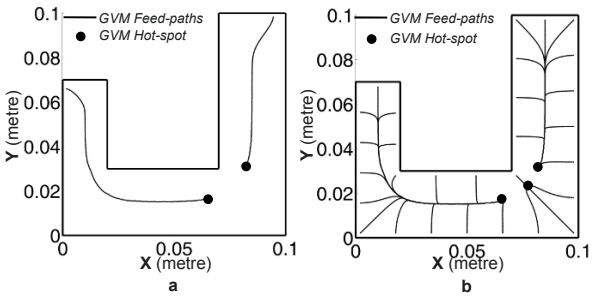

Fig. 4. 'C' shaped casting. a. GVM feed-paths in arms; b. GVM feed-paths from part boundary

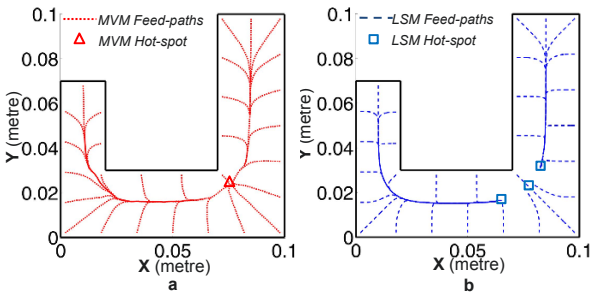

Fig. 5. 'C' shaped casting. a. MVM feed-path; b. LSM feed-path

In the second example, both GVM and MVM feed-path converge to the nearest hot-spots (in the junctions) as shown in Fig. 6. The MVM hot-spots are slightly pulled toward the arm sections. The GVM and MVM hot-spot location differ by about 1% of overall domain dimension. The overlapping plots of feed-paths by GVM and LSM shown in Fig. 7 reveal a close match between feed-path profiles and location of hot-spots.

The computations were performed on a 64-bit Win-XP computer equipped with 2.6 GHz processor and 8 GB RAM. The LSM results took about 105 minutes (excluding pre and post-processing) for a mesh size of 1 mm. Both MVM and GVM results took less than 11 minutes with a step size of 1 mm.

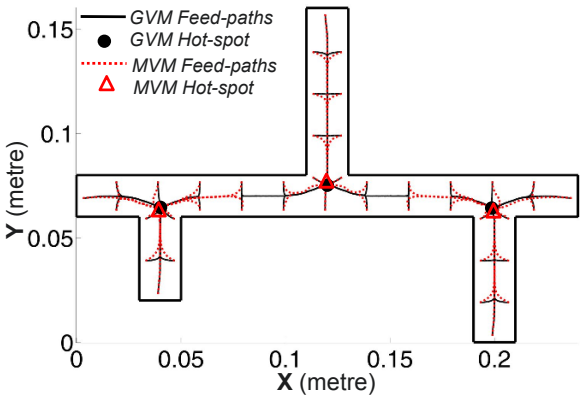

Fig. 6. Multiple junction casting: GVM and MVM results

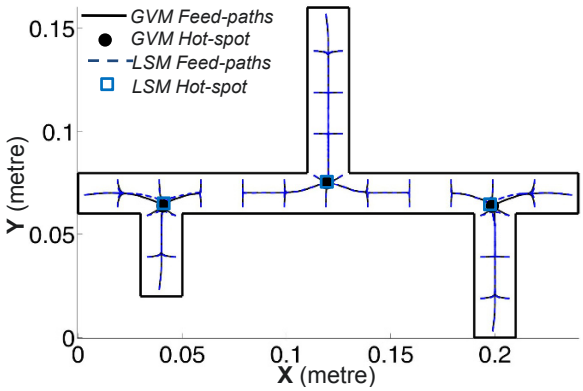

Fig. 7. Multiple junction casting: GVM and LSM results

3.3. Validation by casting

The two castings were produced in sand moulds with the metals mentioned earlier to validate the simulation results. The convergence location of GVM feed-paths in 'C' shaped casting correctly matches with the extended shrinkage cavity observed in the cut-section [(Fig. 8 (a)]. In the multiple-junction casting, three distinct convergence points of feed-paths were identified during simulation. These correctly match the location of shrinkage porosity observed in cut-section [Fig. 8(b)], proving the capability of the method to predict multiple hot-spots.

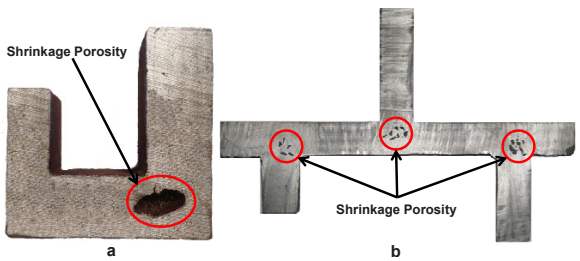

Fig. 8. Cut-section. a. 'C' shaped casting; b. Multiple junction casting

4. Conclusions

Feed-paths provide a better visualization of feeding directions inside a casting compared to the traditional concept of feeding distance, which is essentially based on experimentally-derived empirical expressions for specific metal-mould combinations and limited to simple shapes. The proposed Gradient Vector Method has been shown to accurately compute feed-paths in complex geometries, as well as identify multiple hot-spots. The GVM could correctly identify multiple hot-spots, and its feed-paths are more reliable than those produced by Modulus Vector Method. This is attributed to the fact that the direction of the maximum temperature gradient in GVM is computed from interfacial heat flux, as a function of geometric parameters, material parameters and boundary conditions. It can thus potentially handle material properties and various thermal-boundary conditions encountered in foundries, being based on analytical solution for heat transport equation. Further, the GVM is shown to be about ten times faster than the numerical techniques (level-set-method). This becomes important when different configurations of casting feeders (location, shape, size, etc.) need to be analysed to determine the most optimum one that gives the desired quality at the highest possible yield.

References

[1] Myskowski ET, Bishop HF, Pellini WS, (1952) Application of chills to increasing the feeding range of risers. AFS Transactions 60:389-400

[2] Carslaw HS, Jaeger JC, (1959) Conduction of heat in solids. Oxford University, 2nd edition

[3] Garcia A, Clyne TW, Prates M, (1979) Mathematical model for the unidirectional solidification of metals: II. Massive molds. Metallurgical Transactions B 10:85-92

[4] Voller VR, Cross M, (1981) Accurate solutions of moving boundary problems using the enthalpy method. International Journal of Heat and Mass Transfer 24:545–556

[5] Welch SWJ, Wilson J, (2000) A volume of fluid based method for fluid flows with phase change. Journal of Computational Physics 160:662-682

[6] Chen S, Merriman B, Osher S, Smereka P, (1997) A simple level set method for solving Stefan problems. Journal of Computational Physics 135:8-29

[7] Sutaria M, Gada VH, Sharma A, Ravi B, (2012) Computation of feed-paths for casting solidification using Level-Set-Method. Journal of Material Processing Technology, doi: 10.1016/j.jmatprotec.2012.01.019

[8] Viswanathan S, Duncan AJ, Sabau AS, Han Q, Porter WD, Riemer BW, (1998) Modeling of solidification and porosity in aluminum alloy castings. AFS Transactions 106:411-417

[9] Ravi B, Srinivasan MN, (1996) Casting solidification analysis by modulus vector method. International Cast Metals Journal 9(1):1-7

Effect of casting orientation, thickness and composition on solidification structure and properties of ductile iron castings

V. D. Shinde [1], B. Ravi [2] and K. Narasimhan [3]
[1]Department of Metallurgical Engineering & Materials Science, Indian Institute of Technology Bombay, Mumbai-400076 (India), shinde@iitb.ac.in
[2]Professor, Department of Mechanical engineering, Indian Institute of Technology Bombay, Mumbai-400076 (India)
[3]Professor, Department of Metallurgical Engineering & Materials Science, Indian Institute of Technology Bombay, Mumbai-400076 (India)

Abstract. In this work, the effect of casting orientation (horizontal, vertical), thickness (4-16 mm) and composition (Cu, Mn) were investigated on the mechanical properties (tensile strength, yield strength, elongation, hardness) of hypereutectic ductile iron castings. Thermocouples were placed in the middle of four sections of a step casting. Overall horizontal castings were found to cool faster than vertical castings. Thermal analysis (cooling curves) shows a wide difference among the four sections. Thinner sections exhibited significant undercooling and thereby carbide formation, leading to poor ductility. The combined effect of Cu and Mn gives higher strength with a drop in ductility especially in thin sections, which can be used to balance carbide formation.

Keywords: Thin wall casting, ductile iron, solidification, inoculation, microstructure

1. Introduction

The transportation industry faces three major challenges: control of emissions, improvement of fuel efficiency and reduction of costs. One solution to all these challenges is to reduce vehicle weight; a reduction of 100 kg is commonly equated to a fuel efficiency improvement of 0.4 km per liter [1]. Since castings constitute a significant proportion of vehicle weight, manufacturers are exploring weight reduction by redesigning the castings with thinner walls [2, 3]. It is however, a challenge to produce thin wall ductile iron casting with the desired properties.

Solidification of hypoeutectic ductile iron proceeding below liquidus temperature causes nucleation of austenite; graphite spheroids nucleate on pre-existing austenite and grow in the interdendritic regions. In hypereutectic melts, solidification starts with graphite nodules [4, 5], with subsequent decrease in carbon % in the liquid. Upon further cooling, austenite grows dendritically, allowing new graphite spheroids in interdendritic regions [6]. Graphite nodules nucleate on small inclusions [7] but further growth solely depends on foreign particles or solutes which are added as inoculant [4]. Austenite formed during solidification undergoes solid state transformation while cooling below eutectic temperature, overlapping the solidified structure and making solidification mechanisms more complex [7, 8, 9, 10]. Since it is preferable to have more graphite nodules, especially in thinner sections, hypereutectic ductile irons are preferred for such castings.

The chemical composition, melt treatment and cooling rate are important process parameters which determine the final properties of ductile iron. The graphite nodule count, nodularity (deviation from spherical shape) and the amount of phases are important control parameters to achieve better properties. Melt treatment includes modification and inoculation, in which initially the melt is treated with magnesium alloy (for changing graphite shape from flake to spheroidal) followed by further inoculation (for increasing the nodule count or to suppress carbide formation) to facilitate heterogeneous nucleation [6]. Sufficient graphite nucleation is required in order to avoid formation of carbides due to higher solidification rates in thin wall ductile iron castings [11, 12].

Heat transfer behavior during solidification of actual castings can be studied by inserting suitable thermocouples in the casting cavity. The measured cooling curve reflects the effect of solidification variables such as chemical composition, inoculation and its efficiency [13]. The melt quality is controlled by the chemical composition, pouring temperature, efficiency of inoculation and shrinkage tendency [14].

The commonly measured mechanical properties for ductile iron are tensile strength, yield strength, percent elongation and Brinell hardness. Because of the fairly consistent influence of spheroidal graphite and structure of its base matrix, the tensile properties and the Brinell

hardness of ductile iron are well related. In the matrix, the softer ferrite gives higher ductility but lower strength than pearlite. Also the graphite morphology plays an important role, as the graphite shape deviates from the ideal spherical shape, the ductility and strength reduce [15]. The time after spheroidal treatment has significant effect on elongation, but less effect on the tensile strength and hardness of castings.

Chemical composition plays a vital role in solidification processing of ductile iron. Even small changes of the elements show significant increase or decrease in mechanical properties of ductile iron [16]. Silicon is a strong solid solution strengthener; it reduces undercooling and avoids carbide formation by nucleating graphite. It segregates negatively. Copper and Manganese are pearlite stabilizers. Chromium is a pearlite former as well as a carbide former which leads to segregation. Molybdenum is pearlite stabilizer and promotes hardenability [17, 18]. Arsenic and Tin are subversive elements and hence are kept within controlled limits [4].

During nodularizing, numerous inclusions are formed with a sulphide core and an outer shell containing complex magnesium silicates. After inoculation with a ferrosilicon alloy containing Ca, Ba or Sr, the surface of magnesium silicate micro-particles is modified and other complex silicate layers will be produced [8]. Such silicates have the same hexagonal crystal lattice structure as graphite. Due to very good lattice match they act as effective nucleation sites for graphite nodules to grow from the melt during solidification. The particles with good epitaxial fit between nucleant and graphite embryo are the most potent catalysts to grow graphite [9].

As some of the measured Magnesium is in the form of MgS, the final level of Sulfur affects the Magnesium needed to result in nodular graphite. Maximum nodularity can be achieved by keeping magnesium residual just enough, but decreasing magnesium below 0.02% will deteriorate the nodule shape (spheroicity). Nodule count can be maximized by sound base iron melting along with good inoculation practice [18]. Nodule count and nodularity, both are affected by cooling rate. Thin sections (due to fast cooling) result in better nodule shape than slower cooling sections for the same magnesium residuals.

Previous work shows that for improving the strength of a casting, Copper is an important constituent. Manganese is used in this study for strengthening the casting by promoting pearlitic matrix, but increasing manganese may alter the structure by promoting carbides in different section thicknesses. This effect can be studied by varying the amount of manganese and copper, which balance strength and ductility. Further, the effect of different section thickness and casting orientation for a given composition of ductile iron also needs to be studied. These have been taken up in the present investigation.

2. Experimental work

In the current study, experiments were designed and conducted to study solidification behavior in varying thickness ductile iron castings as shown in Table 1. A step casting was designed with four sections having thickness 4, 8, 12 and 16 mm respectively as shown in Fig. 1. Each step is 50 mm long, making the total length of casting 200 mm. The width of the casting is 100 mm, so as to avoid end freezing effects in all sections. Multiple gates were provided (one in each section of the casting) for rapid and uniform filling. A wooden pattern was fabricated, and used to prepare the molds in green sand. K-type thermocouples were inserted in the middle of each step to record the thermal history of casting solidification. Two castings each with vertical and horizontal orientation are poured and four castings with varying Cu and Mn composition are also cast (Fig. 2). A 16-channel data logger (Ambetronics), capable of storing 2995 readings for each port, was used.

Table 1. Experiments conducted and composition

Melt code	Casting orientation	Composition
V1	Vertical	Trace Cu, 0.2% Mn
V2	Vertical	Trace Cu, 0.2% Mn
H1	Horizontal	Trace Cu, 0.2% Mn
H2	Horizontal	Trace Cu, 0.2% Mn
A	Horizontal	Trace Cu, 0.2% Mn
B	Horizontal	0.2% Cu, 0.3% Mn
C	Horizontal	0.4% Cu, 0.4% Mn
D	Horizontal	0.5% Cu, 0.5% Mn

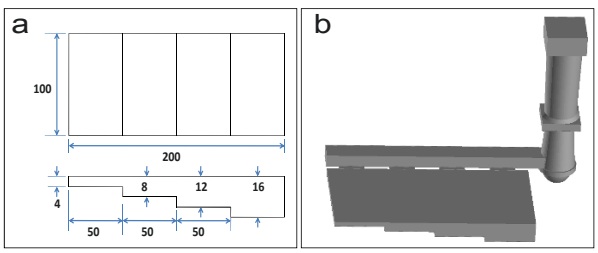

Fig. 1. (a) Details of the step casting, (b) 3D model of step casting

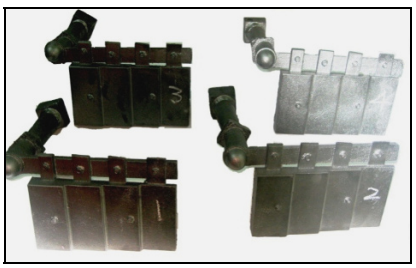

Fig. 2. Horizontal Castings with composition (A, B, C, D)

The melt charge consisted of 50 kg pig iron, 150 kg cold rolled steel scrap and balance foundry returns with suitable chemical composition. The charge mix was melted in 300 kg capacity coreless medium frequency induction furnace. The molten metal was tapped into a preheated ladle containing Ferro-silicon- magnesium (FeSiMg) alloy granules of size 10-15 mm at the bottom covered with steel scrap (sandwich process). The tapping temperature was 1450 ^{o}C.

The inoculant was added in the melt stream while pouring for proper mixing. Inoculant particles were of 2 to 3 mm in size so as to dissolve easily and dust free to avoid oxidation losses. The spectroscopic analysis of the melt samples was carried out just before pouring into the mold, using a spectrometer (BRUKER, model Q-4 Tasman).

The treated iron was poured into mold cavity at a temperature of 1380 ^{o}C for all castings. Four experiments (two vertical and two horizontal castings) were conducted for studying the effect of casting orientation with the same chemical composition. The measured tensile and Brinell hardness readings on each steps of casting H1 were reported in Table 2. The thermocouples were inserted in the castings H2 and V2.

Table 2. Tensile and hardness test results in step casting H1

Thickness (mm)	T. S. (MPa)	0.2% Y.S. (MPa)	Elongation %	BHN
4	426.33	338.83	12.30	207
8	418.43	326.23	13.75	192
12	412.51	317.47	14.87	179
16	394.38	310.72	14.95	177

Another four experiments studied the effect of chemical composition for a given orientation (horizontal). In all the four melts (labeled A, B, C, and D), C=3.6% and Si=2.5-2.78% gave a carbon equivalent of 4.33-4.43, which is in hyper-eutectic range. Cu varied from 0.035 to 0.512% and Mn varied from 0.216 to 0.518% as shown in Table 3. Other elements present in the melt were Pb<0.01, Al=0.006, Cr=0.015, Mo<0.002, Ni<0.002 and Ti=0.02.

Table 3. Spectroscopic analysis of the castings A, B, C, D

Melt No.	C	Si	Cu	Mn	Mg
A	3.62	2.51	0.035	0.216	0.035
B	3.63	2.69	0.214	0.310	0.034
C	3.68	2.68	0.401	0.392	0.032
D	3.61	2.78	0.512	0.518	0.039

3. Results and discussion

The solidification temperature history recorded using thermocouples and stored in the data logger was used to plot the cooling curves for each section thickness (Fig. 3). The amount of undercooling was noted in each graph. In horizontally oriented sections, the under-cooling varied from 18 ^{o}C in thinnest to 5 ^{o}C in thickest sections. In vertically oriented sections, the corresponding variation was from 16 to 8 ^{o}C.

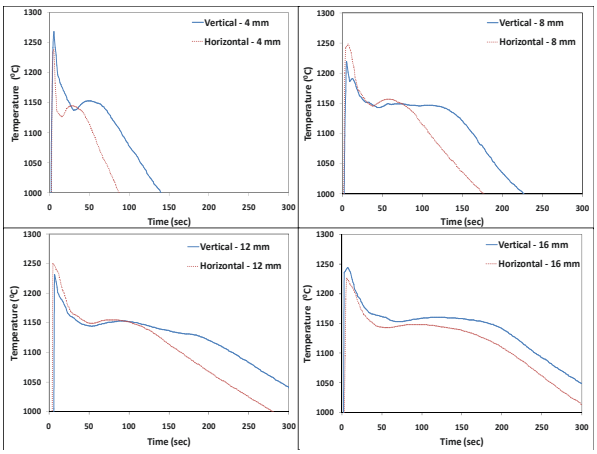

Fig. 3. Cooling curve for vertical and horizontal castings at the center with different wall thickness

Tensile test specimens were prepared from each casting as per ASTM standard E8M-04. The brinell hardness is measured on the samples taken from the middle portion of each casting. The tensile and hardness results are shown in Table 4. The samples for micro-structure studies were taken from the middle portion of the casting and polished. These were etched with 2% Nital (2% concentric Nitric acid and 98 ml Methanol solution). Optical micrographs were taken using a camera attached to a Leintz microscope (Fig.4). The polished samples were studied using an Image Analyzer (Pro-metal-11) for nodule count, nodularity and percentage of ferrite and pearlite content (Table 5).

Table 4. Tensile testand hardness results of the castings

Melt No.	T.S. (MPa)	0.2%Y.S.(MPa)	Elongation %	Hardness (BHN)
A	412.53	307.34	14.87	179
B	456.58	327.73	10.23	187
C	532.46	382.32	7.35	224
D	614.61	417.23	2.85	247

Table 5. Microstructure image analysis of the castings

Melt	Pearlite %	Ferrite %	Nodularity %	Nodule count
A	11.80	88.19	91.07	395
B	24.56	75.40	91.23	330
C	60.12	39.89	88.52	207
D	80.28	19.72	94.68	199

The thermal analysis of the four sections within the horizontal castings indicates faster cooling rate compared to corresponding sections in vertical casting. Irrespective of the orientation, approximately 5% carbides are found in thinner sections. In vertical casting, the metal is not stagnant during mold filling delays the nucleation leading to lesser amount of carbide formation.

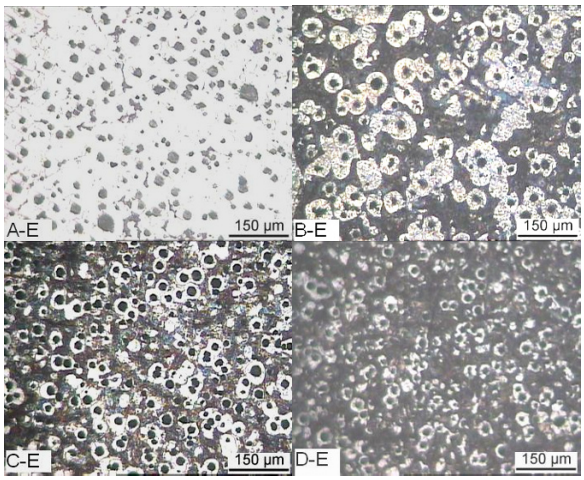

Fig. 4. Microphotographs of ductile iron castings with 2% nital A to D in 12 mm sections etched, labled A-E to D-E respectively

This is more clearly reflected in the cooling curve of 4 mm thin vertically oriented casting. Copper and Manganese promote pearlite and need to be controlled to achieve the desired mechanical properties of ductile iron castings. The effect of copper is to increase the amount of pearlite; manganese stabilizes the pearlite but also promotes carbides. The simultaneous increase of both Cu and Mn enhances both tensile and yield strengths without a significant decrease in ductility (as compared to that observed by an increase in Cu alone). The microstructure study indicates no traces of carbides in 16, 12 and 8 mm sections and only 4 to 5% carbides in 4 mm thick sections.

The nodule size distribution affects shrinkage tendency, since it reflects graphite formation and expansion throughout the entire solidification sequence. Small nodules and uniform distribution indicates an early graphite nucleation which may lead to micro-porosity and wide range of graphite nodule sizes indicating continuous nucleation of graphite while solidification. The amount of under-cooling, which is measure of the energy barrier against heterogeneous nucleation increases with lattice disregistry in the structure of respective regions in the casting.

4. Conclusions

The properties of ductile iron as indicated by their grades are largely determined by their microstructure, which in turn is affected by section thickness of the casting and chemical composition of the melt. Thin wall (4 mm) sections are more prone to deep undercooling and carbide formation, especially in horizontal orientation. The microstructure and thereby mechanical properties (especially tensile strength and ductility) can be improved in thin wall ductile iron castings by simultaneously increasing the amount of copper and manganese. The combined addition of Cu and Mn varying from 0.1 to 0.5% increased the amount of pearlite from 15 to 80% in the ductile iron castings, which in turn increased the strength from 413 to 615 MPa. The corresponding fall in ductility (percentage elongation) was 15% to only 3%.

Acknowledgement: Authors gratefully acknowledge the assistance of Ganesh Foundry, Magna Industries, and S.S. Industries, Ichalkaranji for supporting melting trials, thermal analysis and microstructure analysis.

References

[1] Dogan O, Schrems KK, Hawk JA (2003) AFS Transactions, 111: 949–959.
[2] Bockus S, Venckunas A and Zaldarys G (2008) Materials Science, 14(2): 1392-1320.
[3] Javaid A., Davis K.G. and Sahoo M. (2000), Modern Casting, 6:33-41.
[4] Flemings MC, (1974) Solidification Processing. McGraw-Hill Book Company, New York.
[5] Skaland T (2005) Nucleation mechanisms in cast iron, Proceedings of the AFS Cast Iron, September 29-30, Schaumburg, Illinois,13-30.
[6] Rivera GL, Boeri RE and Sikora JA (2003) AFS Transactions, 111, 979-989.
[7] Skaland T, Grong Ø and Grong T (1993) Metallurgical and Materials Transactions A, 24:2321-2345.
[8] Elliot R, (1988) Cast Iron Technology. Butterworth-Heinemann, Oxford.
[9] Rio Tinto Iron and Titanium, Ductile Iron Databook for Design Engineers, Montreal, 1999.
[10] Campbell J (2004) Castings, Elsevier, Amsterdam.
[11] Stefanescu DM, Ruxanda R and Dix LP (2003) Int. J. Cast Metals Research, 16 (3): 319-324.
[12] Fras E, Gorny M (2007) Archives of Foundry Engineering, 7(4):57-62.
[13] Pedersen KM and Tiedje NS (2008) Materials Characterization, 59:1111-1121.
[14] Sparkman D, (1994) Modern Casting, 84(11):35.
[15] Bockus S, Dobrovolskis A (2004) Materials Science (Medziagotyra), 10(1):1392-1320.
[16] Soinski MS and Derda A (2008) Archives of Foundry Engineering, 8(3):149-152.
[17] Gonzaga RA and Carrasquilla JF (2005) Journal of Materials Processing Technology, 162: 293-297.
[18] Gonzaga RA, Landa PM, Perez A and Villanueva P (2009) Journal of Achievements in Materials and Manufacturing Engineering, 23(2):150-158.

Laser beam shaping for manufacturing processes

Duncan Hand
Institute of Photonics and Quantum Sciences, Heriot-Watt University, Edinburgh EH14 4AS

Abstract. The standard laser beam shape (typically Gaussian or similar) is not always optimal for a particular process. In this presentation the use of adaptive optics (both deformable mirrors and spatial light modulators) to dynamically alter the beam shape is investigated for laser precison machining processes.

Keywords: laser precision machining, laser beam shaping, laser-based manufacturing processes

1. Summary

A particular laser can in general provide a single beam shape, whilst laser-based manufacturing processes often require many different illumination strategies and/or patterns. These can be generated by rapidly moving the focused laser beam relative to the workpiece by means of a high speed optical scanner, trepanning optic, or motorised stages. However, there are applications where this kind of beam manipulation is not sufficient, where it is instead preferable to use spatial beam shaping optics. Such shaping can be achieved with fixed optics, including: masks, diffractive optical elements (DOEs) [1], and phase plates [2]; however the ability to dynamically alter the beam shape offers much increased process flexibility, as well as enabling implementation of speckle reduction techniques (speckle is typically a problem with DOEs). There are various kinds of adaptive optics which can be used in this way, splitting into 2 key types: (i) deformable mirrors and (ii) spatial light modulators. Both can be applied to laser manufacturing processes [3,4], with liquid crystal spatial light modulators having the distinct advantage of being able to operate as either controllable phase plates, DOEs, or amplitude masks. A wide variety of complex beam shapes can therefore be generated at the workpiece (examples are shown in Fig. 1), and these can be dynamically manipulated.

In this presentation the application of dynamic beam shaping techniques to laser precision machining processes will be described, for both nanosecond and picosecond lasers, using green and IR light. The extension of such processing to UV wavelengths will also be discussed. Applications described include structuring of metals, glasses and ablation of thin films.

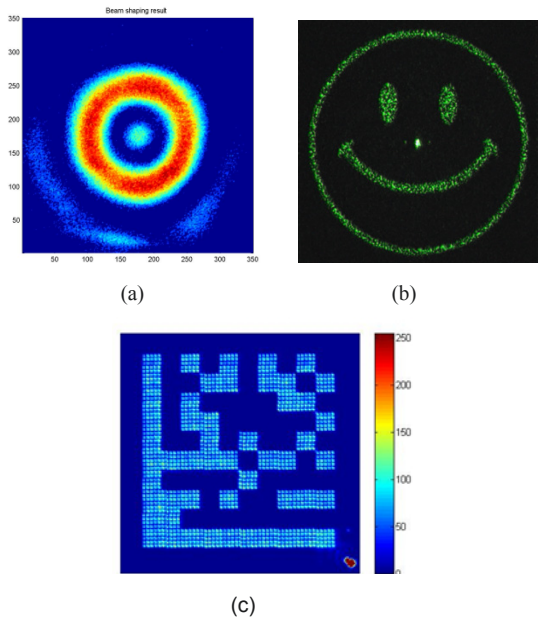

Fig. 1. Example beam shapes produced using liquid crystal spatial light modulators, (a) as a phase plate to generate donut beam at laser focus; (b) and (c) as dynamically variable diffractive optics.

2. Biography

Duncan has been a member of academic staff at Heriot-Watt since 1997. His work on laser-based manufacturing includes laser precision machining; the use of adaptive optics in laser manufacturing processes; and laser joining of microsystems. In this work he collaborates with a range of companies including GE Aviation, Renishaw, BAE Systems and Selex. He has further research activity on the delivery of high peak power laser light through novel optical fibres (with applications in manufacturing and

medicine), including a collaboration with the University of Bath on photonic bandgap fibres. He also has an interest in optical sensing, with current activity in optically-addressed fibre optic micro-cantilever sensors. Duncan is also currently Director of Research for the School of Engineering and Physical Sciences.

References

[1] E. Neiss, M. Flury, J. Fontaine, Diffractive optical elements for laser marking applications - article no. 70032L, in Optical Sensors 2008, F. Bergmans, et al., Editors, Spie-Int Soc Optical Engineering: Bellingham. p. L32 (2008)

[2] A. Bich et al, Multifunctional micro-optical elements for laser beam homogenizing and beam shaping' article no. 68790Q, in Photon Processing in Microelectronics and Photonics Vii, A.S. Holmes, et al., Editors, SPIE-Int Soc Optical Engineering: Bellingham. pp. Q8790-Q8790A (2008)

[3] R.J. Beck, J.P. Parry, W.N. MacPherson, A. Waddie, D.T. Reid, N. Weston, J.D. Shephard, D.P. Hand. Adaptive optics for optimization of laser processing. in Proceedings of LAMP2009 – the 5th International Congress on Laser Advanced Materials Processing. 2009. Kobe, Japan.

[4] Z. Kuang, D. Liu, W. Perrie, S. Edwardson, M. Sharp, E. Fearon, G. Dearden, K. Watkins, Fast parallel diffractive multi-beam femtosecond laser surface micro-structuring. Applied Surface Science, 255(13-14): pp. 6582-6588 (2009)